

1 **Field assessments on impact of CO₂ concentration fluctuations along with complex**
2 **terrain flows on the estimation of the net ecosystem exchange of temperate forests**

3 Dexiong Teng^{1,2}, Jiaojun Zhu^{1,2,3,*}, Tian Gao^{1,2,3}, Fengyuan Yu^{1,2}, Yuan Zhu^{1,2}, Xinhua
4 Zhou^{3,4}, Bai Yang⁴

5 1 CAS Key Laboratory of Forest Ecology and Silviculture, Institute of Applied Ecology, Chinese
6 Academy of Sciences, Shenyang 110000, China

7 2 Qingyuan Forest CERN, National Observation and Research Station, Liaoning Province,
8 Shenyang 110016, China

9 3 CAS-CSI Joint Laboratory of Research and Development for Monitoring Forest Fluxes of Trace
10 Gases and Isotope Elements, Institute of Applied Ecology, Chinese Academy of Sciences,
11 Shenyang 110016, China

12 4 Campbell Scientific Incorporation, Logan, Utah 84321, USA

13 *** Corresponding Author: Jiaojun Zhu**

14 Tel : +86 24 83970342

15 Email: jiaojunzhu@iae.ac.cn

16 **Abstract**

17 The CO₂ storage (F_s) is the cumulation or depletion in CO₂ amount over a period
18 in an ecosystem. Along with the eddy-covariance flux and wind-stream advection of
19 CO₂, it is a major term in the net ecosystem CO₂ exchange (NEE) equation and even
20 dominates in the equation under a stable atmospheric stratification while this equation
21 is used for forest ecosystems over complex terrains. However, estimating the F_s remains
22 challenging due to the frequent gusts and random fluctuations in boundary-layer flows
23 that arouse tremendous difficulties in catching the true trend of CO₂ changes for its
24 storage estimation from eddy-covariance along with the atmospheric profile techniques.
25 Using the measurements from Qingyuan Ker Towers equipped with NEE instrument
26 systems separately covering mixed-broadleaf, oak, and larch forests towers in a
27 mountain watershed, this study investigates the gust periods and CO₂ fluctuation
28 magnitudes while examining their impact on F_s estimation in relation to the terrain
29 complexity index (TCI). The gusts induce CO₂ fluctuations at numerous periods of 1 to
30 10 min over two hours. Diurnal, seasonal, and spatial differences ($P < 0.01$) in the
31 maximum amplitude of CO₂ fluctuations (A_m) ranges from 1.6 to 136.7 ppm and these
32 difference in a period (P_m) at the same significant level ranges 140 to 170 second. The
33 A_m and P_m are significantly correlated to the magnitude and random error of F_s with
34 diurnal and seasonal differences. These correlations decrease as CO₂ averaging time
35 windows becomes longer. To minimize the uncertainties of F_s , a constant [CO₂]
36 averaging time window for the F_s estimates is not ideal. Dynamic averaging time
37 windows and a decision-level fusion model can reduce the potential underestimation of

38 F_s by 29%–33%, being equivalent to 1.9%–4.3% underestimation of the NEE for
 39 temperate forests in complex terrains. The relative contribution of F_s to the 30-min NEE
 40 observations ranged from 17% to 82% depending on turbulent mixing and TCI. The
 41 study's approach is notable as it incorporates TCI and utilizes three flux towers for
 42 replication, making the findings relevant to similar regions with a single tower.

43 **Keywords:** Eddy covariance, complex terrain, carbon flux, storage term, carbon
 44 dioxide concentration, random uncertainty

45 **1 Introduction**

46 The accurate estimation of the net ecosystem exchange (NEE) of carbon dioxide
 47 (CO_2) in forest ecosystems is crucial for a comprehensive understanding of the global
 48 carbon cycle. The eddy covariance (EC) technique has been widely used in forest
 49 ecosystems due to its capacity to directly measure the NEE while measurement
 50 conditions satisfy the underlying theory. The EC technique is based on a simplified
 51 mass conservation equation (after the Reynolds averaging), given by:

$$\begin{aligned}
 \text{NEE} = & \underbrace{\frac{1}{V_m} \int_0^h \left(\frac{\partial \bar{c}}{\partial t} \right) dz}_{\text{I}} + \underbrace{\frac{1}{V_m} (\overline{w'c'})}_h}_{\text{II}} \\
 & + \underbrace{\frac{1}{V_m} \int_0^h \left(\bar{w}(z) \frac{\partial \bar{c}}{\partial z} \right) dz}_{\text{III a}} + \underbrace{\bar{c}(z) \frac{\partial \bar{w}}{\partial z}}_{\text{III b}} dz, \quad (1) \\
 & + \underbrace{\frac{1}{V_m} \int_0^h \left(\bar{u}(z) \frac{\partial \bar{c}}{\partial x} + \bar{v}(z) \frac{\partial \bar{c}}{\partial y} \right) dz}_{\text{IV}}
 \end{aligned}$$

53 where V_m is the volume of dry air in the control volume; c is the CO_2 mixing ratio; t is
 54 the time; h is the measure height; u , v , and w denote the velocity components in the x ,

55 y , and z directions, respectively; and an overbar denotes Reynolds averaging. This
56 equation conceptualizes the NEE within a control volume from the ground to the
57 measurement height (h), while ignoring the horizontal turbulence term divergence
58 (Feigenwinter et al., 2004). In this equation, term I is the CO₂ storage (F_s) representing
59 the change in the average CO₂ concentration (hereafter [CO₂]). Terms II, IIIa, IIIb, and
60 IV represent the vertical turbulent flux (F_c), the vertical advection, the interface vertical
61 mass advection, such as the evaporation process (Webb et al., 1980), and the horizontal
62 advection, respectively.

63 Most flux measurements typically lack the solutions for terms III and IV, and can
64 only estimate the NEE by summing F_c and F_s , and even a significant number of sites
65 ignored the F_s . The F_s in the vertical gas column within a canopy can be substantial,
66 requiring attention in NEE estimates (Aubinet et al., 2000). The F_s contributes ~60% to
67 nocturnal turbulent flux underestimation in forest ecosystems with “ideal” topography
68 (Mchugh et al., 2017). Especially, during atmospherically stable periods such as the
69 early morning, sunset, and nighttime transitions, the F_s has a significant impact on the
70 NEE. For 30-min ecosystem carbon flux measurements, ignoring F_s would
71 underestimate the NEE (Zhang et al., 2010). The F_s value typically ranges from -2 to
72 $-5 \mu\text{mol m}^{-2} \text{s}^{-1}$ in the early morning, and the F_s is about $1-3 \mu\text{mol m}^{-2} \text{s}^{-1}$ after sunset
73 for temperate forests. The effect of the F_s on the NEE of forest ecosystems decreases
74 with the increase of timescale (Li et al., 2020). However, neglecting the F_s value can
75 lead to a misunderstanding of the CO₂ exchange processes, such as ecosystem
76 respiration and photosynthesis, and their relationship with key control factors such as

77 solar radiation, temperature, and moisture (Mchugh et al., 2017). Therefore, it is
78 imperative not to overlook F_s to ensure more precise NEE estimates of forest
79 ecosystems, particularly in complex terrains.

80 Despite the challenges inherent in monitoring forest conditions, understanding the
81 carbon flux of forest ecosystems in complex terrains or with heterogeneous underlying
82 surfaces remains an area of great interest. Topography complexity plays a complex role
83 in the transportation of momentum, energy, and mass in the atmospheric boundary layer,
84 with direct impacts on the airflow patterns, spatiotemporal characteristics, and gas
85 concentration fluctuations (Sha et al., 2021; Finnigan et al., 2020). Differences in
86 airflow along the slope, lateral CO_2 discharge downhill, and spatiotemporal variations
87 in soil respiration result in the CO_2 outflow from slopes and valleys lagging behind the
88 flat top of the mountain (De Araújo et al., 2010). At night, under stable atmospheric
89 stratification, cold air moves from valley forest canopy to the ground the and then flows
90 to low-lying areas, causing a “carbon pooling” effect. The gradient of $[\text{CO}_2]$ below the
91 EC sensors fluctuates significantly, and the cold air discharge above the canopy reduces
92 CO_2 storage, leading to an underestimation of forest ecosystem respiration (Yao et al.,
93 2011; De Araújo et al., 2008; De Araújo et al., 2010).

94 According to the theoretical definition, F_s estimates are derived by averaging the
95 $[\text{CO}_2]$ of the control volume at the beginning and the end of the EC averaging period
96 (30 min or 1 h) and dividing by the EC averaging period (Finnigan, 2006). The
97 estimation of F_s at numerous sites frequently employs a vertical profile system. This
98 approach operates under the assumption that the F_s represents the integration of the time

99 derivative of the vertically determined column-averaged [CO₂]. It is noteworthy that
100 the column-averaged [CO₂] may not accurately represent the average [CO₂] of the
101 control volume in cases of inadequate air mixing, leading to insufficient sampling.
102 Previous study showed that relying solely on tower-top measurements can lead to
103 underestimation of F_s by up to 34% compared to the eight-level profile approach (Gu
104 et al., 2012). The NEE magnitude with the F_s based on the 2-min [CO₂] averaging time
105 window (instantaneous concentration approach) was found to be 5% higher than that of
106 the 30-min-window-based F_s (averaging concentration approach), particularly during
107 nighttime in the growing season (Wang et al., 2016). A proper measuring system with
108 improving the horizontal representativeness can reduce the bias of F_s to 2–10%
109 (Nicolini et al., 2018). Most research has examined how vertical and horizontal gas
110 concentration sampling point distribution affects the uncertainty in F_s estimation
111 (Bjorkegren et al., 2015; Wang et al., 2016; Yang et al., 2007; Yang et al., 1999), with a
112 small number of studies examining the effect of [CO₂] sampling frequency on the F_s
113 (Finnigan, 2006; Heinesch et al., 2007). Certain studies have experimentally validated
114 new concepts, such as correlating the gas sampling point concentration with the
115 horizontal distribution (Nicolini et al., 2018). Some studies have approached the true
116 value theoretically, such as through defining the control volume represented by flux
117 measurements (Metzger, 2018; Xu et al., 2019). However, the number of complete
118 column samples required to describe the column-averaged [CO₂] of each 30-min or 1-
119 h F_s estimate is still undetermined.

120 Previous studies have emphasized the significance of the F_s to the NEE and the

121 influence of [CO₂] dynamics on F_s estimates in complex terrains. To overcome any
122 disparities between sensors and obtain precise changes in the [CO₂] gradient above and
123 below the forest canopy, individual gas analyzers are extensively utilized to measure
124 [CO₂] levels vertically (Siebicke et al., 2011). However, a single gas analyzer introduces
125 time delays when monitoring multi-point [CO₂] curves. Accurately determining the F_s
126 estimates can be challenging due to the spatial and temporal resolution of [CO₂]
127 measurements (Wang et al., 2016). The random error of the F_s estimates using one
128 complete column sample is considerably high due to short-term [CO₂] fluctuations
129 (Nicolini et al., 2018). The calculation of the F_s using time-averaged [CO₂] profiling
130 leads to significant information loss at high frequency, resulting in a substantial
131 underestimation bias. **Furthermore, resource constraints in the measurement system**
132 **leads to the gap that the systematic bias and random error in F_s estimate are**
133 **irreconcilable.** This issue necessitates further efforts to characterize [CO₂] fluctuations
134 across different sites and demonstrate the mechanisms influencing F_s magnitudes,
135 uncertainties, and their contributions to NEE observations in complex terrains. Thus,
136 this manuscript aims to bridge this gap by introducing a statistical method to estimate
137 F_s values and their uncertainties.

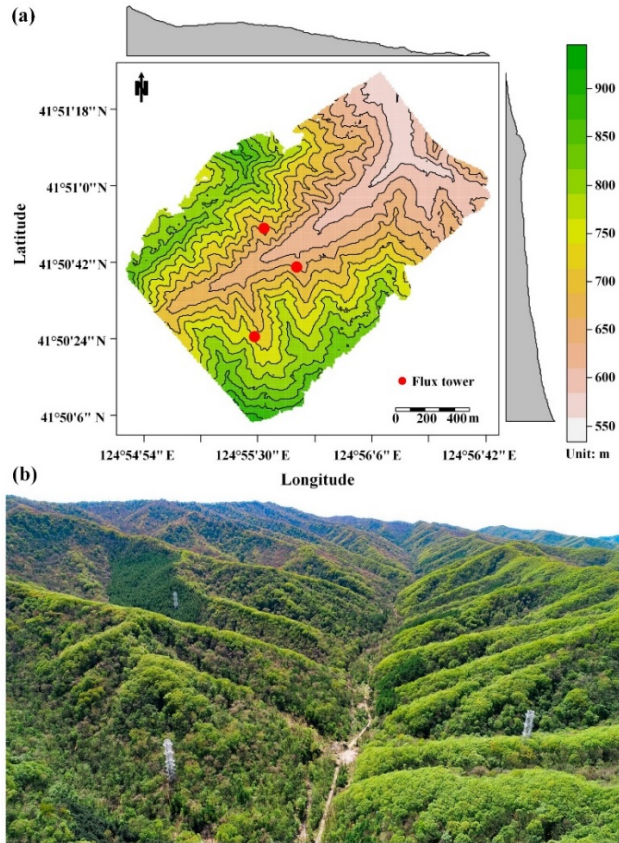
138 This paper employed an innovative EC site with three flux towers (Qingyuan-Ker
139 Towers) to monitor three typical types of temperate forest stands located in complex
140 terrains in northeastern China. This study introduces a decision-level fusion model
141 based on weighing the underestimation bias and random error of the F_s to obtain more
142 accurate results. The objectives of this study were to: 1) compare diurnal, seasonal, and

143 spatial differences in $[\text{CO}_2]$ fluctuations, F_s , and its uncertainty; 2) examine the
144 variation in F_s uncertainty with different $[\text{CO}_2]$ averaging time windows; and 3)
145 investigate the response of F_s and its uncertainty to $[\text{CO}_2]$ fluctuations, wind above the
146 canopy, and terrain complexity, and quantify the impact of the F_s on the NEE estimates
147 under these conditions.

148 **2 Materials and methods**

149 **2.1 Study site and instrumental set-up**

150 This study was conducted in temperate forests in a watershed based on the Ker
151 towers (Zhu et al., 2021; Gao et al., 2020), situated in northeast China ($41^{\circ}50'N$,
152 $124^{\circ}56'E$). The region experiences a temperate continental monsoon climate, with an
153 average annual temperature of 4.3°C and annual rainfall of 758 mm from 2010 to 2021
154 (Li et al., 2023). The Ker towers consist of three 50-m-high EC towers (Fig. 1) that
155 observe a mixed broadleaved forest (MBF), a Mongolian oak forest (MOF), and a Larch
156 plantation forest (LPF).



157

158 Fig. 1 Overview of the study area. The first map (a) depicts the topography of the study site, with
 159 black curves indicating elevation contours, and marginal distributions represented as a gray graph,
 160 averaged over rows and columns. The second image (b) features an aerial photograph of the
 161 Qingyuan-Ker towers captured in the growing season (Gao et al., 2020).

162 The basic information regarding Ker towers in this study is presented in Table 1.

163 The CPEC310 integrated system from Campbell Scientific comprising an EC155
 164 closed-path infrared gas analyzer (IRGA) and a CSAT3A sonic anemometer, was
 165 employed to monitor the three-dimensional wind speed and CO₂/H₂O concentrations
 166 (10 Hz). The atmospheric profiling system (AP200, Campbell Scientific Ltd., Logan,
 167 UT, USA) was utilized to measure the CO₂/H₂O concentrations with eight height levels.
 168 Each level was measured for 15 s (with 10 s for the flushing of the manifold and 5 s for
 169 logging the average), leading to a measurement cycle of 2 min.

170 Table 1 Basic information of Ker towers

Forest	Mixed broad-leaved	Mongolian oak	Larch plantation
Experiment period	Jan 01, 2020– Dec 31, 2021	Jan 01, 2020– Dec 31, 2021	Jan 01, 2020– Dec 31, 2021
Elevation (m)	634	669	721
Slope (°)	14.8 ± 2.1	19.1 ± 2.9	16.2 ± 5.3
Canopy height (m)	21.5 ± 1.8	13.9 ± 0.6	19.5 ± 0.6
Leaf area indices	3.0 ± 0.5	3.1 ± 0.8	3.9 ± 0.6
Eddy covariance system	CPEC310	CPEC310	CPEC310
Eddy covariance sensor height (m)	46	46	36
Atmospheric profiling system	AP200	AP200	AP200
Profile heights (m)	0.5, 2, 6, 11, 16, 21, 26, 36	0.5, 2, 6, 11, 16, 21, 26, 36	0.5, 2, 6, 11, 16, 21, 26, 36

171 2.2 Calculation of storage flux

172 Averaging the [CO₂] in a time window was utilized to calculate the F_s values, in
 173 addition to data on the air pressure, CO₂/H₂O molar fractions, and air temperature at
 174 different heights above the ground surface (Finnigan, 2006; Montagnani et al., 2018;
 175 Xu et al., 2019). The molar mixing ratio and mass mixing ratio are conserved quantities
 176 with the variation of air temperature, air pressure, and water vapor concentration,
 177 whereas the molar fraction is not. This study determined the F_s using the molar mixing
 178 ratio obtained from CO₂/H₂O molar fraction observations, applying the ideal gas law
 179 and Dalton’s partial pressure law (Montagnani et al., 2009). The water vapor molar
 180 mixing ratio (χ_v) in mmol mol⁻¹ is given by

$$\chi_v = \frac{c_v}{1 - c_v \times 10^{-3}}, \quad (2)$$

181 where c_v is the water vapor molar fraction in mmol mol^{-1} , and the CO_2 molar mixing
 182 ratio (χ_c) in $\mu\text{mol mol}^{-1}$ is given by

$$\chi_c = \frac{c_c}{1 - c_v \times 10^{-3}}, \quad (3)$$

183 where c_c is the CO_2 molar fraction in $\mu\text{mol mol}^{-1}$.

184 The dry air density ($\bar{\rho}_d$) in mol m^{-3} is calculated as follows:

$$\bar{\rho}_d = \frac{\bar{P}}{(\bar{T} + 273.15) \times (R^* + \chi_v \times 10^{-3} \cdot R^* \cdot M_d/M_v)}, \quad (4)$$

185 where R^* is the air gas constant ($8.31441 \text{ Pa m}^3 \text{ K}^{-1} \text{ mol}^{-1}$), \bar{P} is the air pressure in
 186 Pa, and \bar{T} is the average air temperature in Celsius. M_d and M_v are the dry air and
 187 water vapor molar mass ($18.015 \text{ g mol}^{-1}$), respectively. M_d is calculated from the CO_2
 188 molar mixing ratio (Khélifa et al., 2007):

$$M_d = 28.9635 + M_c \cdot (\chi_c \times 10^{-6} - 0.0004), \quad (5)$$

189 where M_c is the carbon molar mass ($12.011 \text{ g mol}^{-1}$).

190 The F_s estimated from eight-level profiles are calculated as follows:

$$F_s = \bar{\rho}_d \int_0^h \frac{d\bar{\chi}_c}{dt} dz \doteq \bar{\rho}_d \sum_{i=1}^8 \frac{\Delta\bar{\chi}_{c_i} \Delta h_i}{\Delta t}, \quad (6)$$

191 where $\bar{\chi}_c$ is the average CO_2 molar mixing ratio and Δh_i is the height represented by
 192 each level.

193 When measuring the F_s by sampling CO_2 at several levels using a single analyzer,
 194 the synchronous observations of CO_2 profile are impractical. Consequently, discrete
 195 temporal sampling and time averaging become necessary. To ensure the temporal
 196 alignment of F_s with F_c , the average $[\text{CO}_2]$ measurements within the control volume at
 197 the beginning and end (t) of an averaging period (30 min) are calculated by averaging
 198 over a time window (τ min) as follows:

$$\bar{\chi}_{c_i} = \frac{2}{\tau} \sum_{t-\frac{\tau}{2} < t \leq t+\frac{\tau}{2}} \chi_{c_i}(t), \quad (7)$$

199 where $\tau = 4, 8, \dots, 28$ min. Theoretically, the time window should be kept as short as
 200 possible in comparison to the turbulence flux averaging period to comply with the
 201 principle of Reynolds decomposition. We use large windows here for CO₂ averaging in
 202 an attempt to demonstrate the effects of different window sizes on the accuracy of
 203 storage flux estimates.

204 2.3 Data analysis

205 To evaluate the impact of [CO₂] fluctuations on F_s measurements and its
 206 corresponding uncertainty, empirical modal decomposition (EMD) and Fourier
 207 spectrum analysis were used to extract the period and amplitude of fluctuations in the
 208 high-frequency [CO₂] time series (10 Hz). EMD was used to decompose the [CO₂] time
 209 series into intrinsic mode functions based on local signal properties, which yield
 210 instantaneous frequencies as functions of time, allowing for the identification of
 211 embedded structures of eddies. EMD is applicable to non-linear and non-stationary
 212 processes (Huang et al., 1998). The period and amplitude of [CO₂] fluctuations above
 213 the forest canopies reflected the eddy size. Subsequently, the maximum period and
 214 amplitude of [CO₂] fluctuations in a short term (2h) was indicative of large eddies under
 215 the influence of gust.

216 Due to the diurnal and seasonal variability of flux measurements, this study
 217 defined the transition period and growing season. The solar elevation angle was used
 218 to define the transition period as 1-h before sunrise (sunset) to 2-h after sunrise (sunset).

219 The growing degree days (GDDs) were calculated using the base temperature (T_{base}) to
220 determine the beginning and end of the growing season, and the formula was as follows
221 (Mcmaster and Wilhelm, 1997):

$$GDD = \frac{1}{2}(T_{max} + T_{min}) - T_{base}, \quad (8)$$

222 where T_{base} is 6°C. Considering the persistent demand of temperature to support
223 vegetation growth, the fourth day of the first GDD greater than zero (less than zero)
224 over a span of five consecutive days was defined as the starting (ending) time of the
225 growing season.

226 The main data processing and analysis steps are outlined below:

227 1. EMD and Fourier spectrum analysis of $[CO_2]$ high-frequency time series were
228 used to extract the maximum amplitude (A_m) and corresponding period (P_m) of $[CO_2]$
229 fluctuations every 2 h. The data were divided into two subsets based on P_m , with a cut-
230 off of 150 s.

231 2. CO_2 storage fluxes were calculated for different $[CO_2]$ averaging time windows
232 (τ), ranging from 4 to 28 min in increments of 4 min.

233 3. The standardized major axis (SMA) regression model (Warton et al., 2012) was
234 used to compare the slope differences (bias) between F_{s_τ} and $F_{s_{28}}$ for different P_m and
235 the forest stands. The SMA model offers routines for comparing parameters a and b
236 among groups for symmetric problems.

237 4. The normalized root mean square error (NRMSE) and slope were used to
238 evaluate the relative error and bias between F_{s_τ} and $F_{s_{28}}$. The NRMSE is calculated as
239 follows:

$$NRMSE = 100 \times \sqrt{\frac{\sum_{i=1}^N (F_{s,\tau}^{(i)} - F_{s,28}^{(i)})^2}{\sum_{i=1}^N (F_{s,28}^{(i)} - \overline{F_{s,28}})^2}} \quad (9)$$

240 where i indicates the i^{th} observation.

241 5. The normalized weighting coefficient (w) of $F_{s,\tau}$ was estimated based on the
 242 NRMSE and slope (Wang et al., 2020). The details are shown in Appendix A1. Then,
 243 using the decision-level fusion model, F_{s_comb} was calculated as follows:

$$F_{s_comb} = w_1^* \cdot F_{s_4} + w_2^* \cdot F_{s_8} + \dots + w_7^* \cdot F_{s_28} \quad (10)$$

244 The decision-level fusion model automatically assigned weights to the F_s based on
 245 different $[\text{CO}_2]$ averaging time windows. Its purpose in this study was to balance the
 246 relative error and bias of F_s estimates caused by $[\text{CO}_2]$ sampling. The analysis was
 247 performed using the EMD and smatr R packages (Warton et al., 2012; Huang et al.,
 248 1998).

249 2.4 Uncertainty analysis

250 To improve the accuracy of estimating the uncertainty of F_s using individual tower,
 251 this work has made modifications to the 24-h difference method by extending the
 252 sampling time windows and applying meteorological condition constraints (Hollinger
 253 and Richardson, 2005). This method trades time for space to estimate the uncertainty
 254 of F_s . To determine the uncertainty of F_s , expressed as $\sigma(\varepsilon_s)$, in this case, we compared
 255 the observations at moment i within a day to the average of several observations during
 256 a similar period and with similar meteorological conditions. The specific computations
 257 were as follows:

$$\bar{F}_s^{(i)} = \frac{1}{N} \sum_{t \in \Omega, \lambda_t \in \Lambda} I(\lambda_t) \cdot F_s^{(t)}, \quad (11)$$

$$\Lambda = \{\lambda_t | \sqrt{\frac{(u_*^{(\lambda_t)} - u_*^{(i)})^2}{\sigma_{u_*}} + \frac{(\text{Ta}(\lambda_t) - \text{Ta}^{(i)})^2}{\sigma_{\text{Ta}}} + \frac{(\text{H}(\lambda_t) - \text{H}^{(i)})^2}{\sigma_{\text{H}}}} < \delta\}, \quad (12)$$

$$\varepsilon_s^{(i)} = F_s^{(i)} - \bar{F}_s^{(i)}, \quad (13)$$

$$\bar{\varepsilon}_s^{(i)} = \frac{1}{N} \sum_{t \in \Omega, \lambda_t \in \Lambda} I(\lambda_t) \cdot \varepsilon_s^{(t)}, \quad (14)$$

$$\sigma(\varepsilon_s)^{(i)} = \sqrt{\frac{1}{N} \sum_{t \in \Omega, \lambda_t \in \Lambda} I(\lambda_t) \cdot (\varepsilon_s^{(t)} - \bar{\varepsilon}_s^{(i)})^2}, \quad (15)$$

258 where Ω was the moment interval ($i-0.5$ h, $i+0.5$ h) within a certain time window (15
 259 d); I was indicator function; the set Λ represented consisted of elements that meet
 260 similar meteorological conditions, including the u_* , air temperature (Ta), and sensible
 261 heat flux (H); σ_{u_*} , σ_{Ta} , and σ_{H} are the standard deviation of the u_* , Ta, and H,
 262 respectively; δ was the threshold of Euclidean distance; and ε_s was the random error
 263 of F_s .

264 After estimating the uncertainty of F_s , this study extended the work conducted by
 265 Richardson et al. (2008) to analyze its relationship with the magnitude of flux
 266 measurements ($|F_s|$), $[\text{CO}_2]$ fluctuations (A_m and P_m), u_* , and terrain complexity index
 267 (TCI). A comprehensible description of the TCI can be found in Appendix A2. This
 268 relationship can be approximated by using the following equation:

$$\sigma(\varepsilon_s) = \beta_0 + \sum_{i=1} \beta_i \cdot x_i, \quad (16)$$

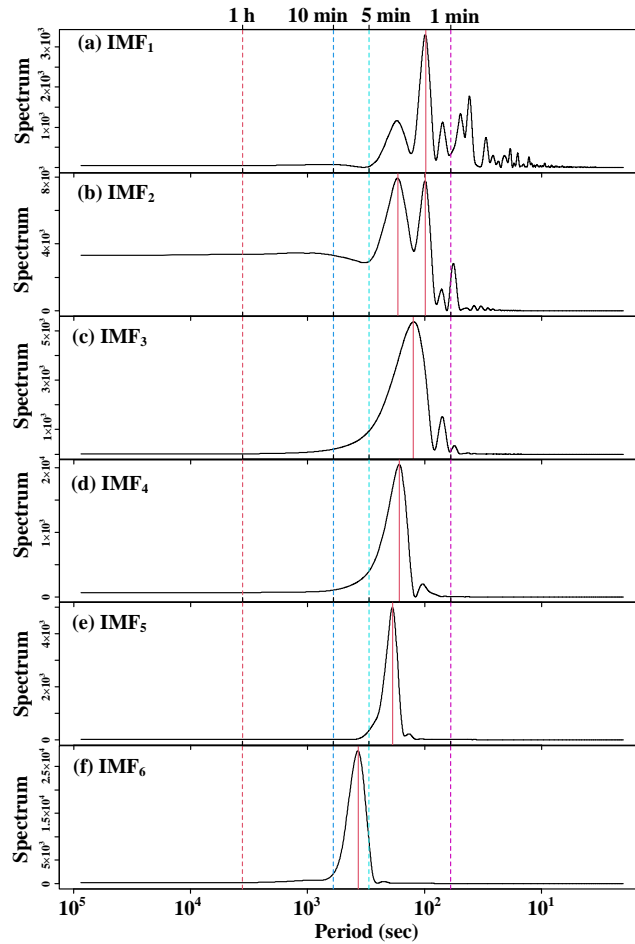
269 where the nonzero intercept term β_0 indicates the size of the random uncertainty as
 270 x_i approaches 0, which varies with the observation site, with larger value of β_0

271 indicating greater uncertainty. The slope term β_i indicates the sensitivity of the size of
272 the random uncertainty of x_i , with smaller β_i values indicating a probability
273 distribution of uncertainty closer to white noise.

274 **3 Results**

275 3.1 Characterization of [CO₂] fluctuation and F_s variations

276 The [CO₂] high-frequency time series above the forest canopies were decomposed
277 using EMD, followed by spectral analysis to extract the fluctuation period and
278 amplitude of [CO₂] at different time scales. As depicted in Fig. 2, it became evident that
279 the [CO₂] above the canopies displayed short-term fluctuations with periods ranging
280 from 1 to 10 min, and the amplitude of these fluctuations showed an increasing trend
281 with longer periods. This observation strongly suggested the presence of large eddies
282 influenced by gusts above the canopies, and these eddies were responsible for the
283 increasing amplitude of [CO₂] fluctuations as their size increased.



284

285 Fig. 2 Power spectral density of the intrinsic mode function (IMF) of above-canopy CO₂
 286 concentrations in the Mongolian oak forest on July 2, 2020 (24 h).

287 To examine the spatio-temporal variations in large eddies, this study compared the
 288 A_m and P_m values above canopies across different forest stands. The analysis utilized
 289 data from daytime, nighttime, and transition periods in both the growing and dormant
 290 seasons. The averages of A_m and P_m averages for the above-canopy [CO₂] in the three
 291 forest stands ranged from 1.588 to 136.667 ppm and from 2.313 to 2.784 min,
 292 respectively (Table 2). Fig. 3 demonstrated significant seasonal and diurnal differences
 293 ($P < 0.01$) in P_m , with higher values during daytime in the growing season, and lower
 294 values during the daytime in the dormant season. Moreover, P_m was significantly
 295 different ($P < 0.01$) among different forest stands during the same time period, with

296 MBF stand having the highest values, followed by the MOF, and the lowest values in
 297 the LPF. During the growing season, the A_m values were significantly higher than those
 298 during the dormant season, with both daytime and nighttime values also exhibiting
 299 significant differences ($P < 0.01$) among different forest stands. This observation
 300 provided evidence of significant spatio-temporal variability in large eddies influenced
 301 by gusts.

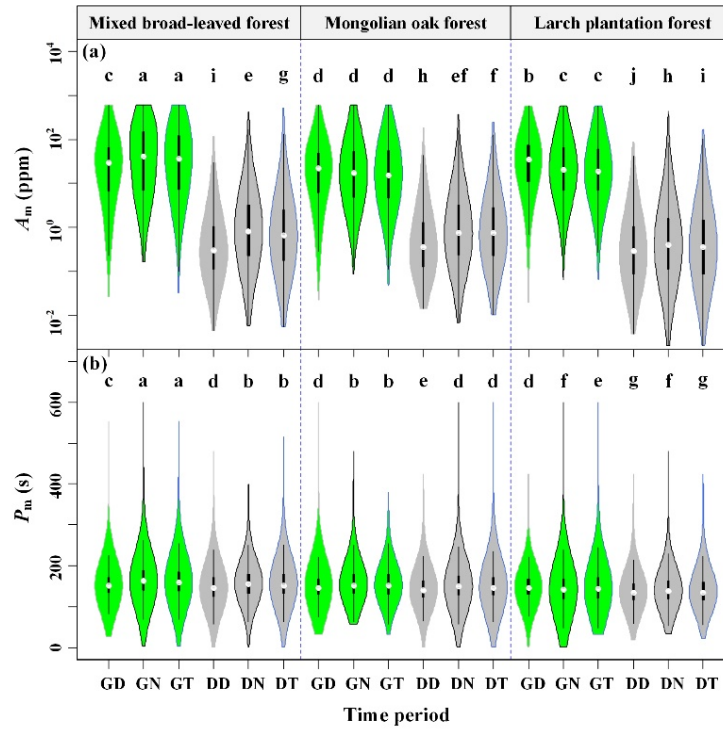
302 Table 2 Mean of the A_m and P_m in different forest stands at different periods

Variable	Tower site	Growing season			Dormant season		
		DT ¹	NT ²	TP ³	DT	NT	TP
A_m ⁴ (ppm)	MBF ⁶	57.932	139.667	136.717	2.219	5.212	4.944
	MOF ⁷	36.160	57.945	55.777	2.699	5.175	4.637
	LPF ⁸	52.688	58.816	60.147	1.588	2.985	2.456
P_m ⁵ (s)	MBF	154.563	167.024	164.824	158.449	151.428	158.121
	MOF	151.986	160.633	159.146	153.091	147.491	153.274
	LPF	149.003	143.950	145.696	143.458	138.794	142.009

303 ¹ DT represents daytime; ² NT represents nighttime; ³ TP represents transition period. ⁴ A_m
 304 represents the maximum amplitude of short-term CO₂ concentration fluctuations; ⁵ P_m represents
 305 the corresponding period of maximum amplitude. ⁶ MBF represents mixed broad-leaved forest; ⁷
 306 MOF represents Mongolian oak forest; ⁸ LPF represents Larch plantation forest.

307 To estimate the uncertainty of F_s using an individual tower, a comprehensive
 308 analysis of its diurnal and seasonal dynamics, as well as the functional relationship
 309 between F_s and u^* , was necessary. Fig. 4 presented significant diurnal variations and
 310 seasonal differences in F_s across the three forest stands. During the growing season, the
 311 median diurnal variation of F_s for the three forest stands ranged from -2.960 to 2.647
 312 $\mu\text{mol m}^{-2} \text{s}^{-1}$, whereas during the dormant season, it ranged from -1.306 to 1.012 μmol
 313 $\text{m}^{-2} \text{s}^{-1}$. Comparing the **extent** of F_s diurnal variation among the three forest stands,

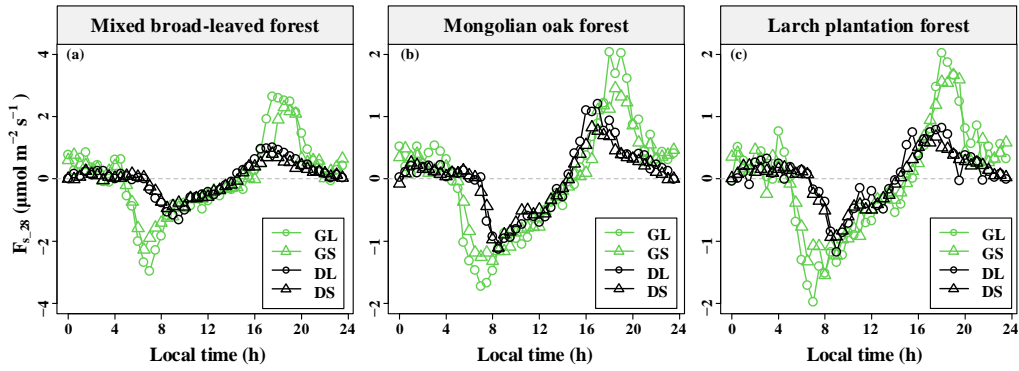
314 MBF exhibited the largest **extent** during the growing season, while the **extent** of the
 315 three forest stands were similar during the dormant season. Notably, it was observed
 316 that the amplitudes for longer P_m values were greater than those for shorter P_m values.
 317 This observation indicated that the larger the eddies, the greater the magnitude of F_s .



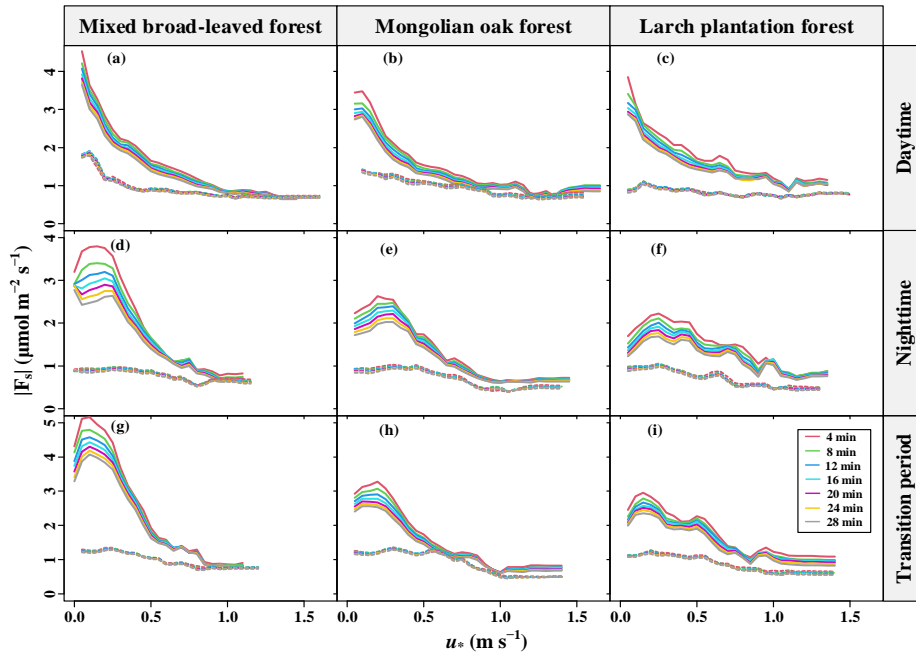
318
 319 Fig. 3 Maximum amplitude (A_m) (a) and corresponding period (P_m) (b) of short-term CO_2
 320 concentration fluctuations in different forest stands for seasonal and diurnal variations, where GD,
 321 GN, GT, DD, DN, and DT denote the growing season daytime, growing season nighttime,
 322 growing season transition period, dormant season daytime, dormant season nighttime, and
 323 dormant season transition period, respectively. Columns with different lowercase letters are
 324 significantly different ($P < 0.05$) according to Fisher's least significant difference test.

325 Furthermore, a u^* threshold value was identified for the variation of F_s with u^*
 326 during daytime in both the dormant and growing seasons (Fig. 5). When u^* fell below
 327 the u^* threshold, the magnitude of F_s ($|F_s|$) decreased with increasing u^* . Conversely,
 328 when u^* exceeded the u^* threshold, the $|F_s|$ tended to remain relatively constant. Notably,
 329 a maximum point for the $|F_s|$ was observed when the u^* was less than 0.5 m/s during the

330 growing season, whereas not during the dormant season. This phenomenon was
 331 particularly evident during the nighttime and transition periods of the growing season,
 332 where $|F_s|$ exhibited an initial increase followed by a subsequent decrease with u^* . These
 333 observations strongly indicated that the effect of the turbulent mixing strength on the
 334 $|F_s|$ over complex terrains was nonlinear and exhibited diurnal and seasonal differences.



335
 336 Fig. 4 Median diurnal variation of CO₂ storage flux (F_s) based on 28-min CO₂ concentration
 337 averaging time windows in the three forest stands during different seasons. GS indicates the
 338 growing season and a short period of maximum amplitude (P_m), GL indicates the growing season
 339 and a long P_m , DS indicates the dormant season and a short P_m , and DL indicates the dormant
 340 season and a long P_m .



341
 342 Fig. 5 Magnitudes of CO₂ storage flux ($|F_s|$) determined with different CO₂ concentration average
 343 time windows as a function of the friction velocity (u^*) and moving block averages from all 30-

344 min data for the years 2020-2021. Dashed and solid lines indicate the dormant and growing
345 seasons, respectively.

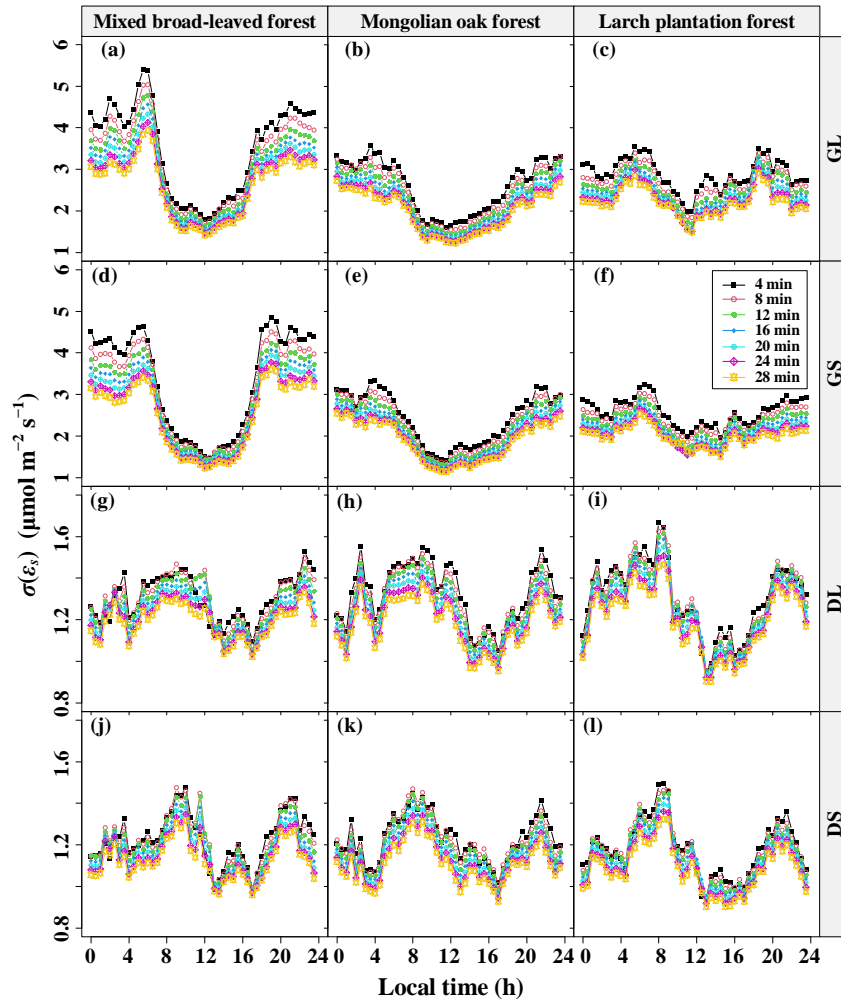
346 3.2 Effect of [CO₂] fluctuations on the F_s and its uncertainty

347 To investigate the influence of the [CO₂] fluctuation periods on the error of F_s
348 measurement, this study computed the diurnal average of the standard deviation $\sigma(\varepsilon_s)$
349 of the 30-min F_s uncertainty (ε_s) separately for different P_m values and the seasons. The
350 overall distribution of ε_s showed a non-normal distribution with a high peak (kurtosis >
351 2 and $P < 0.05$, results presented in Supplementary Table 1–4). The daily variation
352 curves of $\sigma(\varepsilon_s)$ at various [CO₂] averaging time windows are presented in Fig. 6. It
353 was observed that the diurnal variation range of $\sigma(\varepsilon_s)$ was higher during the growing
354 season compared to the dormant season, regardless of the P_m lengths, indicating a
355 seasonal difference independent of the P_m . Additionally, during the growing season,
356 both MBF and MOF demonstrated evident diurnal variation in $\sigma(\varepsilon_s)$, with the peak
357 occurring at night and the trough during the daytime. The diurnal variation range of
358 $\sigma(\varepsilon_s)$ varied across the three forest stands, with MBF exhibiting the largest amplitude.

359 Furthermore, a significantly positive correlation was observed between $\sigma(\varepsilon_s)$ the
360 |F_s| ($P < 0.01$), with site, seasonal, and diurnal differences (Fig. 7). The relationship
361 between these variables was characterized by intercepts and slopes that varied across
362 different [CO₂] averaging time windows, ranging from 1.99 to 2.82 and from 0.24 to
363 0.28, respectively (results presented in the Supplementary Tables 5–6). Both decreased
364 as the [CO₂] averaging time window increased, with the growing season exhibiting
365 larger values compared to the dormant season (results shown in the Supplementary

366 Tables 5–6). These findings suggested that increasing the [CO₂] averaging time window,
367 results in a reduction of the random error in F_s and the correlation coefficient between
368 $\sigma(\varepsilon_s)$ and |F_s|. This indicated a decrease in variability of $\sigma(\varepsilon_s)$ and a behavior similar
369 to white noise.

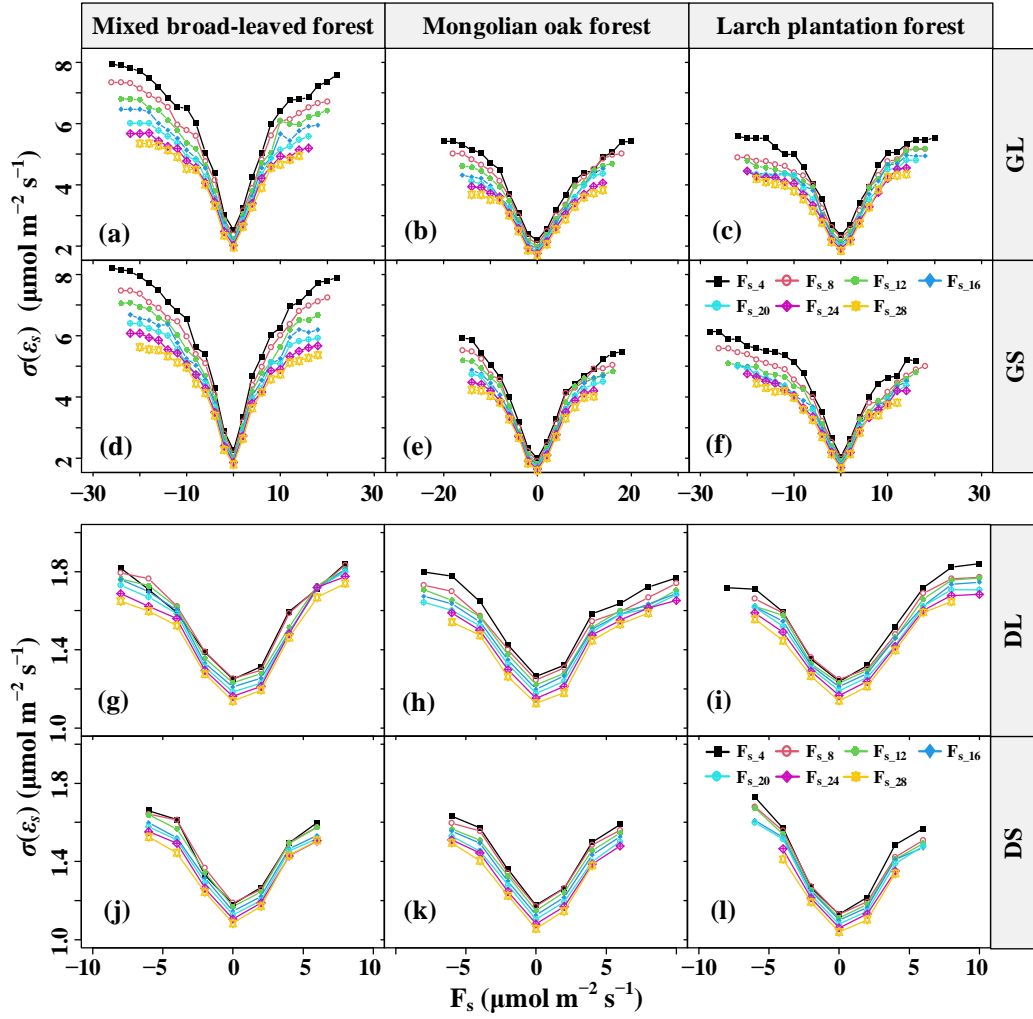
370 To assess the impact of [CO₂] fluctuations on the error and bias of F_s measurement,
371 this study compared the NRMSE and slopes of F_s based on different [CO₂] averaging
372 time windows, with reference to the baseline F_{s,28}, across various P_m values, time
373 periods, and sites. As shown in Fig. 8, the NRMSE decreased and approached
374 convergence as the [CO₂] averaging time windows increased. During both daytime and
375 nighttime in the growing season, the NRMSE corresponding to longer P_m was greater
376 than that corresponding to shorter P_m, while the opposite trend was observed during the
377 dormant season. Additionally, the longer the [CO₂] averaging time window, the greater
378 the relative underestimation of F_s.



379

380 Fig. 6 Diurnal variations in the random uncertainty ($\sigma(\varepsilon_s)$) of CO₂ storage flux (F_s) errors (ε_s) at
 381 different CO₂ concentration ($[CO_2]$) averaging time windows and their seasonal differences, where

382 GS indicates the growing season and a short period of maximum amplitude (P_m) of $[CO_2]$
 383 fluctuations, GL indicates the growing season and a long P_m , DS indicates the dormant season and
 384 a short P_m , and DL indicates the dormant season and a long P_m .



385

386

387

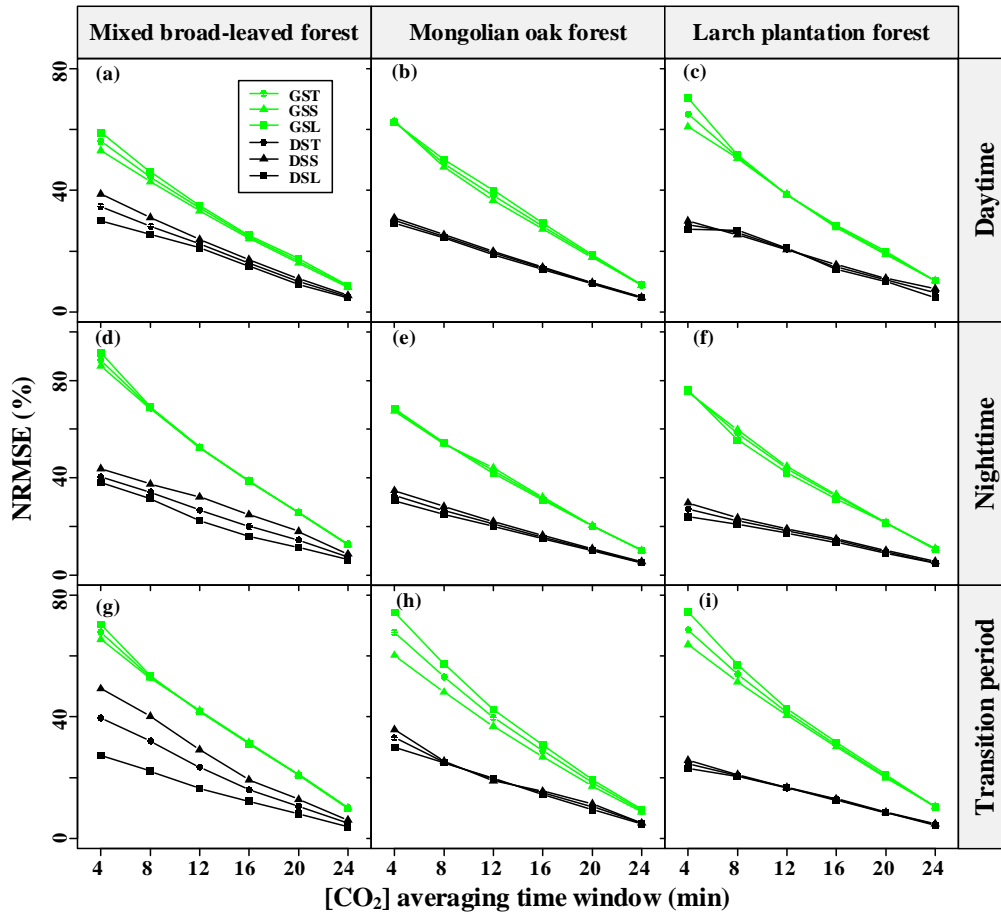
388

389

390

391

Fig. 7 Random uncertainty $\sigma(\varepsilon_s)$ of CO_2 storage flux (F_s) errors (ε_s) at different CO_2 concentration ($[\text{CO}_2]$) averaging time windows as a function of the F_s magnitude for mixed broad-leaved forest, Mongolian oak forest, and Larch plantation forest during the growing and dormant seasons. GS indicates the growing season and a short period of maximum amplitude (P_m) of $[\text{CO}_2]$ fluctuations, GL indicates the growing season and a long P_m , DS indicates the dormant season and a short P_m , and DL indicates the dormant season and a long P_m .



392

393

394

395

396

397

398

399

Fig. 8 Seasonal and diurnal differences in the normalized root mean square error (NRMSE) of F_s versus the respective $F_{s,28}$ values for different CO_2 concentration ($[CO_2]$) averaging time windows. GST indicates the growing season and does not distinguish the period of maximum amplitude (P_m) of $[CO_2]$ fluctuations, GSS indicates the growing season and a short P_m , GSL indicates the growing season and a long P_m , DST indicates the dormant season and does not distinguish P_m , DSS indicates the dormant season and a short P_m , and DSL indicates the dormant season and a long P_m .

400

401

402

403

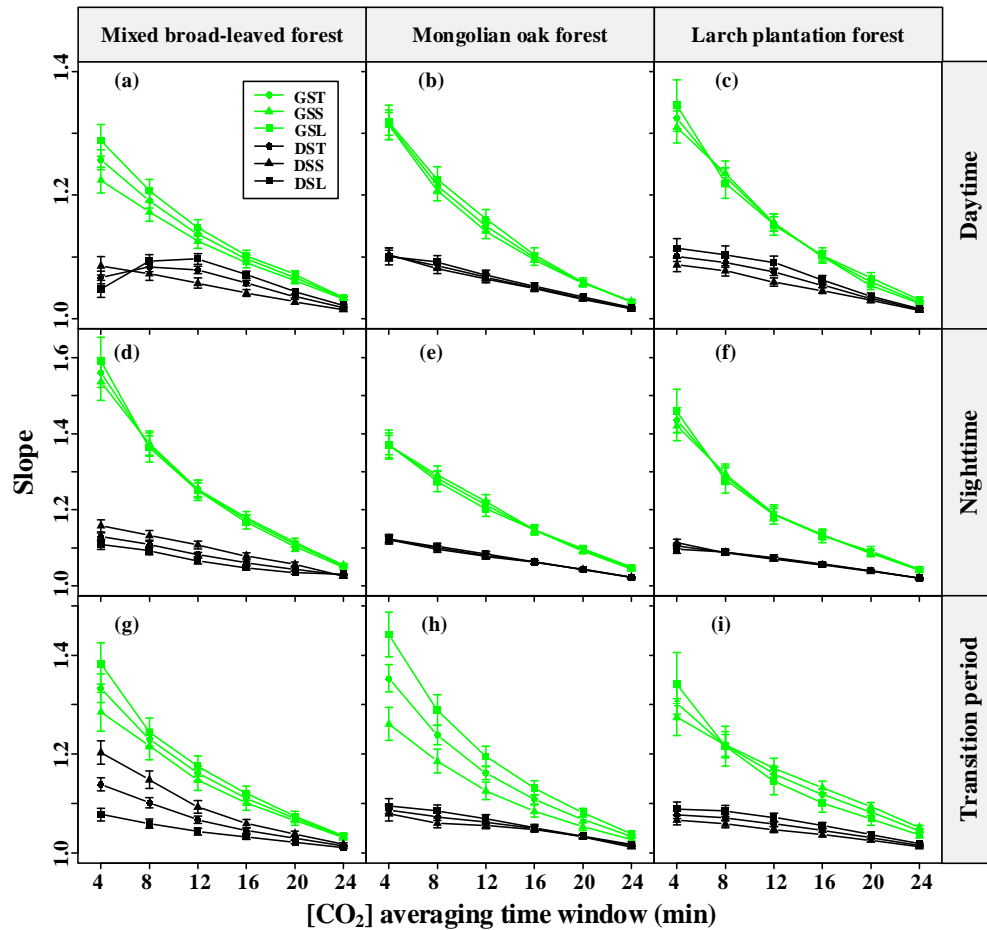
404

405

406

The comparison of slopes between $F_{s,4}$ and $F_{s,28}$ in the three forest stands revealed interesting patterns, as depicted in Fig. 9. During the growing season, the slopes corresponding to the shorter P_m of $[CO_2]$ fluctuations were consistently lower than those for the longer P_m , indicating that the effect of P_m on F_s uncertainty decreased with increasing $[CO_2]$ averaging time windows. However, for the MBF stand (Fig. 9d and Fig. 9g), the slopes corresponding to the shorter P_m of $[CO_2]$ fluctuations during the dormant season nighttime were actually greater than those for the longer P_m , primarily

407 due to diurnal variations in the daily dynamics of F_s . Overall, the influence of P_m on F_s
 408 uncertainty decreased with increasing $[CO_2]$ averaging time windows. This suggested
 409 that averaging $[CO_2]$ reduced the effect of gusts on the random uncertainty in estimating
 410 F_s , but led to a systematic underestimation of F_s .



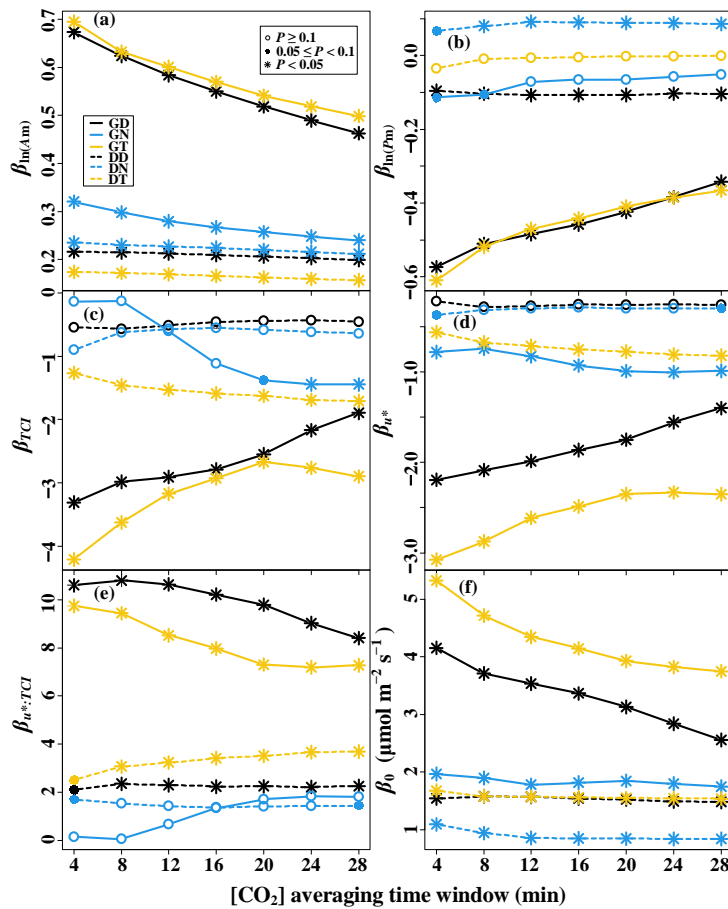
411
 412 Fig. 9 Seasonal and diurnal differences in the slope of CO_2 storage flux (F_s) versus the $F_{s,28}$ for the
 413 different CO_2 concentration ($[CO_2]$) averaging time windows. GST indicates the growing season
 414 and does not distinguish the period of maximum amplitude (P_m) cases, GSS indicates the growing
 415 season and a short P_m , GSL indicates the growing season and a long P_m , DST indicates the
 416 dormant season and does not distinguish P_m , DSS indicates the dormant season and a short P_m ,
 417 and DSL indicates the dormant season and a long P_m .

418 To analyze the effect of $[CO_2]$ fluctuations on $|F_s|$ in complex terrains, this study
 419 developed a multiple linear regression model, considering the interaction effects of
 420 turbulent mixing and terrain complexity on $|F_s|$, as shown in Fig. 10. A_m exhibited a

421 significant positive correlation with $|F_s|$ in all time periods ($P < 0.05$). Conversely, P_m
422 showed a significant negative correlation with $|F_s|$ during the dormant season daytime,
423 the growing season daytime, and the transition periods ($P < 0.05$). Additionally, their
424 correlation coefficient decreased with increasing τ . In Fig. 10d and Fig. 10e, a u^*
425 threshold was observed during the growing season nighttime. When the u^* was below
426 the threshold, higher TCI values resulted in smaller $|F_s|$; whereas when the u^* was above
427 the threshold, higher TCI values led to larger $|F_s|$. During the growing season nighttime
428 and transition periods, u^* showed a significant negative correlation ($P < 0.05$) with $|F_s|$,
429 and the correlation coefficient decreased with increasing TCI values. These
430 observations suggested that the effect of turbulent mixing on the $|F_s|$ uncertainty was
431 regulated by terrain complexity.

432 A multiple linear regression model was used to analyze the effect of $[CO_2]$
433 fluctuations on the random uncertainty of F_s , $\sigma(\varepsilon_s)$, in complex terrains. This model
434 considered the interaction effects of $[CO_2]$ fluctuations and terrain complexity on
435 $\sigma(\varepsilon_s)$, as shown in Fig. 11. As evident from Fig. 11a and Fig. 11e, the A_m exhibited a
436 significant positive correlation ($P < 0.05$) with $\sigma(\varepsilon_s)$ during both the dormant season's
437 nighttime and the growing season. Throughout the transition period of the growing
438 season, P_m displayed a significant negative correlation with $\sigma(\varepsilon_s)$ ($P < 0.05$). The
439 magnitude of these correlation coefficients decreased with the increasing $[CO_2]$
440 averaging time windows. During the transition period of the dormant season, a TCI
441 threshold was observed, with P_m showing a significant positive correlation ($P < 0.05$)
442 with $\sigma(\varepsilon_s)$ when the TCI was below the threshold, and a significantly negative

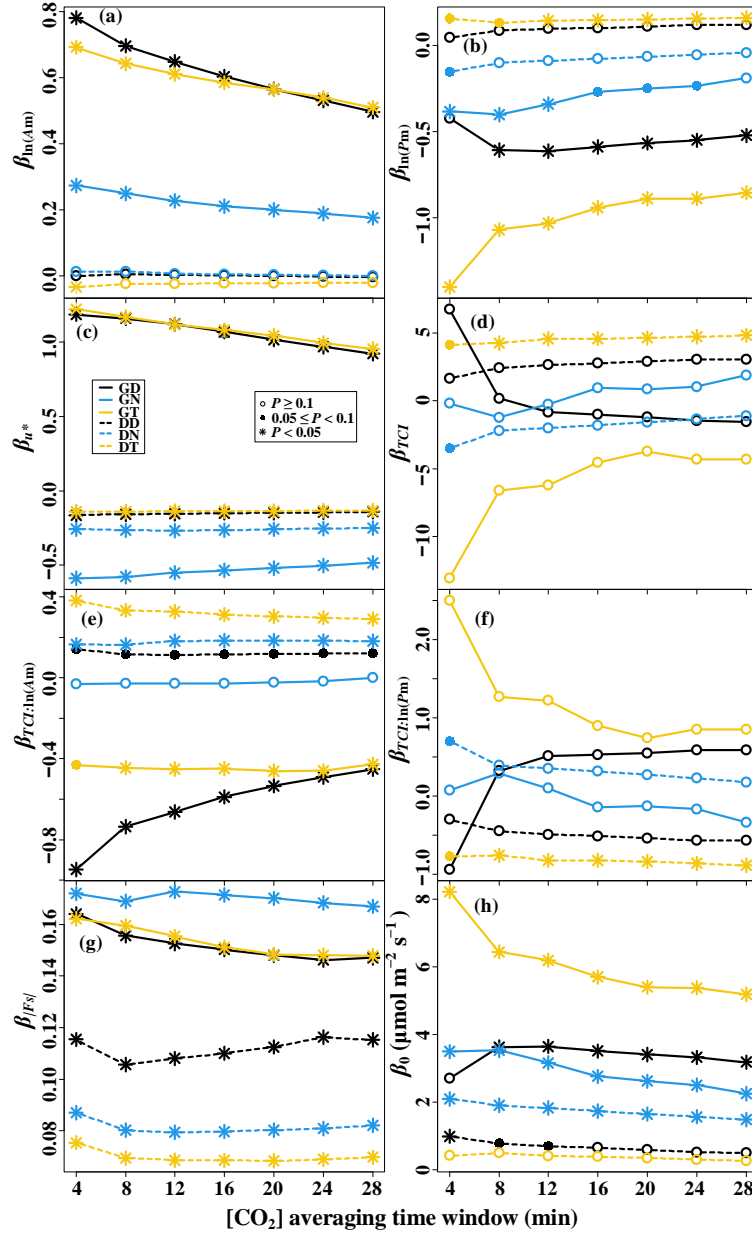
443 correlation ($P < 0.05$) with $\sigma(\varepsilon_s)$ when the TCI exceeded the threshold (Fig. 11b and
 444 Fig. 11f). The u^* showed a significantly negative correlation with $\sigma(\varepsilon_s)$ during the
 445 daytime and transition periods of the growing season ($P < 0.05$), while in other time
 446 periods, u^* was significantly positively correlated with $\sigma(\varepsilon_s)$ ($P < 0.05$). The $|F_s|$
 447 demonstrated a significant positive correlation with $\sigma(\varepsilon_s)$ ($P < 0.05$) in all time
 448 periods, with its correlation coefficient being greater during the growing season than
 449 during the dormant season. **These observations suggested that the relationship between**
 450 **the random uncertainty in F_s and $[CO_2]$ fluctuations was moderated by topographic**
 451 **complexity. Increasing the $[CO_2]$ averaging time window reduced the effect of $[CO_2]$**
 452 **fluctuations on the random uncertainty in F_s .**



453

454 Fig. 10 Linear regression coefficients of the CO_2 storage flux (F_s) magnitude—driving factors

455 relationships for the seven CO₂ concentration ([CO₂]) averaging time windows. The predictors of of
 456 the multiple linear models are (a) the logarithm of maximum amplitude of [CO₂] fluctuations
 457 (ln(A_m)), (b) the logarithm of the corresponding period of maximum amplitude (ln(P_m)), (c) the
 458 terrain complexity index (TCI), (d) the friction velocity (u*), and (e) the interaction term of TCI
 459 and u*, respectively. (f) β₀ represents the intercept term.

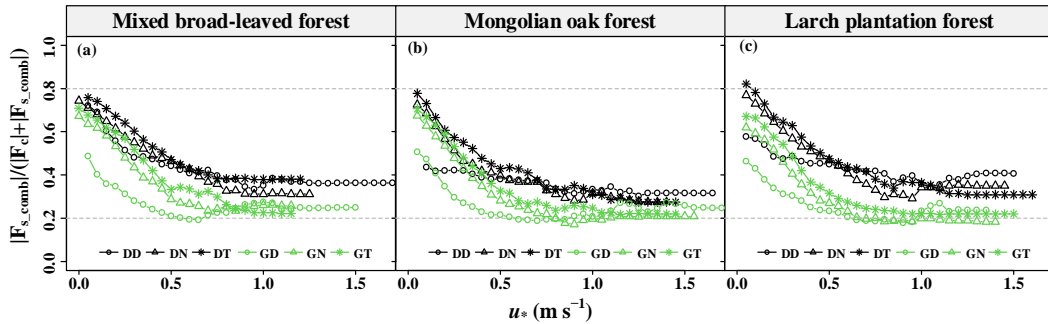


460
 461 Fig. 11 Linear regression coefficients of the random uncertainty of CO₂ storage flux ($\sigma(\epsilon_s)$)—
 462 driving factors relationships determined with Eq. (11) for the seven CO₂ concentration ([CO₂])
 463 averaging time windows. The predictors of the multiple linear models are (a) the logarithm of
 464 maximum amplitude of [CO₂] fluctuations (ln(A_m)), (b) the logarithm of the corresponding
 465 period of maximum amplitude (ln(P_m)), (c) the terrain complexity index (TCI), (d) the friction velocity

466 (u^*), (e) the interaction term of TCI and $\ln(A_m)$, (f) the interaction term of TCI and $\ln(P_m)$, and the
 467 magnitude of storage flux ($|F_s|$), respectively. (h) The intercept term is represented by β_0 .

468 3.3 Effect of CO₂ storage fluxes uncertainty on NEE observations

469 The 30-min F_{s_comb} was obtained by weighing the bias and random error of F_s using
 470 different [CO₂] averaging time windows and P_m values. This study then focused on the
 471 magnitude of F_{s_comb} in relation to the F_c magnitude and its diurnal, seasonal, and site
 472 variations. To assess the significance of F_s in NEE observations, the relative
 473 contribution ratio of F_{s_comb} magnitude ($|F_{s_comb}|/(|F_c|+|F_{s_comb}|)$) was employed. The
 474 $|F_{s_comb}|/(|F_c|+|F_{s_comb}|)$ showed a decreasing trend to convergence with increasing u^*
 475 (Fig. 12). On average, the $|F_{s_comb}|/(|F_c|+|F_{s_comb}|)$ ranged from 17.2% to 82.0%, with a
 476 higher value during the dormant season compared to the growing season. This indicated
 477 that as turbulence intensity increased, the contribution of F_s to the NEE in forests
 478 decreased to a constant value. Nevertheless, even under strong turbulence intensity, F_s
 479 still played a significant role in the NEE observations of forests in complex terrains.



480
 481 Fig. 12 Relative contribution ratio of the CO₂ storage flux magnitude ($|F_{s_comb}|/(|F_c|+|F_{s_comb}|)$)
 482 determined by decision-level fusion model as a function of the friction velocity (u^*) moving block
 483 averages from all 30-min data for the years 2020–2021. GD represents the growing season's
 484 daytime; GN represents the growing season's nighttime; GT represents the growing season's
 485 transition period; DD represents the dormant season's daytime; DN represents the dormant
 486 season's nighttime; DT represents the dormant season's transition period.

487 As indicated in Table 3, both P_m and TCI exhibited a significant positive

488 correlation with $|F_{s_comb}|/(|F_c|+|F_{s_comb}|)$ ($P < 0.05$), while both A_m and u^* showed a
489 significant negative correlation with $|F_{s_comb}|/(|F_c|+|F_{s_comb}|)$ ($P < 0.05$). Notably,
490 seasonal variations in correlation coefficients were observed. The correlation between
491 the u^* and $|F_{s_comb}|/(|F_c|+|F_{s_comb}|)$ was more pronounced during both the dormant
492 season's transition period and the growing season, and it decreased with increasing TCI
493 values during the dormant season's daytime and nighttime.

494 Table 3 Linear regression coefficients of the relative contribution ratio of F_{s_comb}
495 magnitudes to NEE observations ($|F_{s_comb}|/(|F_c|+|F_{s_comb}|)$) —driving factors
496 relationships for the six time periods.

Time period	β_0	$\ln(P_m)^7$	$\ln(A_m)^8$	u^*^9	TCI ¹⁰	$u^*:TCI$	R^2
Total	0.292 ***	0.048 ***	-0.037 ***	-0.334 ***	0.790 ***	-1.018 ***	0.278 ***
GD ¹	0.299 ***	0.016	-0.041 ***	-0.183 ***	-0.293 *	0.239	0.158 ***
GN ²	0.370 ***	0.029	-0.023 ***	-0.386 ***	-0.038	0.081	0.103 ***
GT ³	0.161	0.060 ***	-0.014 ***	-0.182	1.056 ***	-1.754	0.186 ***
DD ⁴	0.393 ***	0.011	-0.020 ***	-0.154 *	0.306	-0.153	0.040 ***
DN ⁵	0.661 ***	0.012	-0.026 ***	-0.443 ***	-0.035	0.399	0.088 ***
DT ⁶	0.495 ***	0.017	-0.036 ***	-0.294 ***	0.564	-0.852	0.149 ***

497 ¹ GD represents the growing season's daytime; ² GN represents the growing season's nighttime;
498 ³ GT represents the growing season's transition period; ⁴ DD represents the dormant season's
499 daytime; ⁵ DN represents the dormant season's nighttime; ⁶ DT represents the dormant season's
500 transition period. ⁷ A_m : maximum amplitude; ⁸ P_m : corresponding period of maximum amplitude. ⁹
501 u^* : friction velocity; ¹⁰ TCI: terrain complexity index; *** represents $P < 0.001$; ** represents $P <$
502 0.01; and * represents $P < 0.05$.

503 To evaluate the impact of F_{s_comb} on NEE_{obs} ($F_c + F_s$), we further evaluated the
504 slope (with intercept terms forced to zero) and NRMSE of $F_c + F_{s_comb}$ compared to F_c
505 + F_{s_28} , as presented in Supplementary Materials Table 7 and Table 8. The F_{s_28} in the
506 three forest stands was underestimated by 28.6%–33.3% compared to the F_{s_comb} , and
507 the NRMSE of F_{s_comb} versus the F_{s_28} ranged from 59.2% to 67.2%. The NEE_{obs} with
508 F_{s_28} was underestimated by 1.9%–4.3% compared to the NEE_{obs} with F_{s_comb} . The
509 NRMSE of NEE_{obs} with the F_{s_comb} versus the F_{s_28} in the three forest stands ranged
510 from 16.0% to 25.4%. The analysis suggested that combining the F_s values based on
511 different averaging [CO₂] time windows in the decision-level fusion model could
512 successfully weigh potential underestimation bias and random uncertainties.

513 The influences of F_s on the relationship between NEE observations and
514 meteorological drivers, indicated the effect of uncertainty in F_s estimates on NEE
515 observations. Our analysis showed that the correlations between NEE observations
516 derived from F_c+F_s and both photosynthetic photon flux density (PPFD) and air
517 temperature are lower compared to those obtained from F_c alone (Figure 1 and Figure
518 2 in the Supplementary Materials). Additionally, the estimated light saturated net CO₂
519 assimilation (A_{max}) is greater when NEE observations are estimated by F_s+F_c , as
520 opposed to when NEE is estimated solely by F_c . This suggests that F_s significantly
521 affects daytime NEE and can correct the estimation of A_{max} and related parameters. The
522 relationship between NEE observations and PPFD is influenced by the size of averaging
523 time window the F_s measurement. A larger averaging window results in less random
524 uncertainty in the F_s estimation, thereby increasing the correlation between NEE

525 observations and meteorological drivers, including PPFD and T_a .

526 **4 Discussion**

527 4.1 Short-term $[CO_2]$ fluctuations above the forest canopy and F_s estimates in complex
528 terrains

529 Compared to flat and uniform underlying surface, complex terrain and
530 heterogeneous canopies modify the trajectory, speed distribution and direction of the
531 airflow. Increased wind speeds and shifting wind directions also increase turbulent
532 activity above the canopy, facilitating the mixing and dispersion of CO_2 . This study
533 found that short-term fluctuations of $[CO_2]$ above the canopy exhibited a range of 1 to
534 10 min (Fig. 2). These fluctuations were characterized by an average P_m ranging from
535 2.313 to 2.784 min (Table 2). Our results are in line with previous research using
536 wavelet analysis, which reported fluctuation periods of $[CO_2]$ within and above the
537 forest canopy to be between 14 and 116 s (Cava et al., 2004). Their observations of the
538 canopy waves during periods of extreme atmospheric stability (when $z/L \gg 1$) exhibited
539 a dominant period of 1–2 min, consistent with our findings. The period of $[CO_2]$
540 fluctuations was found to be predominantly influenced by turbulent fluxes and the
541 residence time of CO_2 within the canopy. This indicated a potential correlation between
542 P_m and the residence time of CO_2 within the canopy. Fuentes et al. (2006) employed a
543 Lagrangian model and calculated the residence time of air parcels released near the
544 ground and canopy, finding values ranging from 3 to 10 min and from 1 to 10 min,
545 respectively. Similarly, Edburg et al. (2011) used the standard deviation of $[CO_2]$

546 averages to determine CO₂ residence time at different locations, including the ground,
547 within the canopy, and in their gas mixtures, yielding values of 8.6, 3.6, and 5.6 min,
548 respectively. The results of these simulation experiments are consistent with our study,
549 further supporting the association between [CO₂] fluctuations above the forest canopy
550 and CO₂ residence time.

551 Tree density and canopy structure also play a role in influencing the air parcel
552 residence time; in flat terrains, the air parcel residence time correlate with u^* (Gerken
553 et al., 2017), and an increase in vegetation leaf area leads to longer residence times
554 when turbulence is not fully penetrative. During the growing season, forests exhibit
555 higher leaf area index and canopy densities compared to the dormant season, resulting
556 in longer P_m of short-term [CO₂] fluctuations above the canopy (Fig. 3). Additionally,
557 at night, stable atmospheric conditions lead to longer residence times due to suppressed
558 turbulent mixing, resulting in relatively long nighttime P_m values compared to daytime
559 and transition periods (Fig. 3).

560 Complex terrains introduce complex changes in air flow structures, including
561 gravity-induced waves, drainage, and nonlinear waves induced by single gusts, leading
562 to dramatic [CO₂] fluctuations. These dynamics contribute to uncertainties in estimating
563 F_s . During nighttime, long-wave radiation emitted from the valley soil surface leads to
564 the cooling and downslope acceleration of air near the soil surface due to gravity,
565 potentially causing katabatic flow. As inertia-driven upslope winds are halted by
566 katabatic acceleration, a local shallow drainage flow is established, reaching a quasi-
567 equilibrium state approximately 1.5 h after sunset (Nadeau et al., 2013). Under stable

568 atmospheric conditions, even gentle slopes (around 1°) can generate strong gravity-
569 driven waves (Belušić and Mahrt, 2012). Consequently, advection may complicate the
570 interpretation of nighttime EC measurements at certain relatively gentle sites, but this
571 complexity is not evident during daytime measurements (Leuning et al., 2008).
572 Advection plays a role in depleting the CO_2 accumulated within the canopy, resulting
573 in lower F_s fluxes and establishing an inverse relationship between storage and
574 advection (Van Gorsel et al., 2011). The occurrence of larger F_s values for long P_m
575 values suggests weaker advection compared to short P_m values (Fig. 4). In our study,
576 we observed that the F_s magnitude was relatively large during nighttime and transition
577 periods, while it was smaller during daytime (Fig. 4), which is consistent with the
578 findings reported by Wang et al. (2016).

579 **The terrain complexity and the diversity within the canopy significantly affect the**
580 **airflow separation in the atmospheric boundary layer. This results in weakened air**
581 **circulation within the canopy and spatial variation in the patterns and extent of airflow**
582 **separation (Grant et al., 2015).** During nighttime and transition periods in a closed
583 canopy, the turbulent coupling state above and below the canopy gradually decouples,
584 eventually reaching complete decoupling as the u^* decreases (Fig. 5). However, this
585 decoupling does not lead to stable stratification within the canopy. Despite the
586 occurrence of decoupling and advection in the closed canopy, waves are unlikely to
587 exist within the canopy itself (Van Gorsel et al., 2011). As a result, a consistent trend
588 in the variation of F_s with τ is observed across the three forest stands during the growing
589 season, independent of P_m (Fig. 9). Conversely, in an open canopy where waves are

590 present, the observations of F_s become more complex. This complexity could be the
591 primary reason why the variation of F_s with $[CO_2]$ averaging time windows differs
592 between the three forest stands for short P_m values during the dormant season daytime
593 (Fig. 9). The presence of waves introduces additional variability in the measurements,
594 leading to differences in F_s estimates based on different $[CO_2]$ averaging time windows
595 in these particular conditions.

596 4.2 Uncertainty in forest ecosystem F_s measurement in complex terrains

597 The random uncertainty of F_s shares similarities with NEE estimation. For
598 example, the magnitude of F_s measurements is positively correlated with the standard
599 deviation of random uncertainty in F_s . Additionally, the overall distribution of F_s
600 measurements exhibits a non-Gaussian distribution with a high peak, aligning with the
601 statistical properties of NEE uncertainty (Richardson et al., 2006; Richardson et al.,
602 2008). **The uncertainty in the storage term depends a lot on the set-up used, together**
603 **with the biological activity of the ecosystem, and the height of the control volume.** In
604 addition, various factors contribute to the uncertainty in F_s estimates, including flux
605 measurement footprint variations, sampling frequency, spatial sampling resolution of
606 CO_2/H_2O concentrations, and instrumental measurement accuracy. The uncertainty
607 arising from variations in the flux measurement footprint is considerable, typically on
608 the order of tens of percentages, which is an order of magnitude higher than typical
609 sensor errors (Metzger, 2018). The AP200 atmospheric profiling system used in this
610 study has an accuracy of $\pm 0.5 \mu mol mol^{-1}$ and $\pm 0.1 mmol mol^{-1}$ for CO_2 and H_2O
611 concentration measurements, respectively (Montagnani et al., 2018). **The AP200 adopts**

612 **buffer volumes to mix the gas.** Efforts to reduce random errors in [CO₂] originating
613 from pressure fluctuations include adding buffer volumes before IRGA pumping tests
614 (Marcolla et al., 2014). **The buffer volumes are fully mixed during gas extraction and**
615 **performs a weighted average of [CO₂] instantaneous measurements to minimize the**
616 **sampling error for each level's [CO₂] measurement (Cescatti et al., 2016).**

617 The F_s estimates can be influenced by singular eddies that penetrate inside the
618 canopy (Finnigan, 2006). Accurate calculation of F_s requires considering the period of
619 [CO₂] fluctuations with the eddy coherence structure. The spectral energy of the F_s time
620 series is primarily concentrated between 0.001 and 0.2 Hz (500 and 5 s, respectively).
621 However, even with sampling frequencies of 2 Hz and below, significantly lower F_s
622 values are obtained (Bjorkegren et al., 2015). The Nyquist-Shannon sampling theorem
623 dictates that accurate measurements of [CO₂] require a sampling period no longer than
624 half the period of [CO₂] fluctuations. Consequently, to monitor short-term changes in
625 [CO₂], measurements must be taken over a period no longer than half of the period
626 corresponding to the maximum amplitude (or major energy) of [CO₂] fluctuations. In
627 this study, the average P_m for [CO₂] fluctuations fell within the range of 2.313–2.784
628 min (Table 2). Therefore, it is crucial to ensure that the sampling period for [CO₂] does
629 not exceed 1.256 to 1.392 min, which corresponds to half the average P_m range.
630 Monitoring fluctuations of P_m for less than 4 min during a 2-min monitoring period of
631 [CO₂] presents a significant challenge. This is a primary reason that the systematic bias
632 and random error in F_s estimate with a single profile system are irreconcilable (Wang
633 et al., 2016). Short-term [CO₂] fluctuations are mainly influenced by boundary layer

634 turbulence, and sampling errors in incomplete fluctuation cycles will be superimposed
635 with the real advection flux (anisotropy) dispersion in complex terrains (Van Gorsel et
636 al., 2011). This substantially increases the random uncertainty in F_s based on shorter
637 $[CO_2]$ averaging time windows (Fig. 6 and Fig. 8). As a result, the deviation of NEE
638 estimates from the actual value expands.

639 **Fluxes in heterogeneous regions are significantly higher than in uniform regions.**
640 **The energy transfer from the ground surface to large eddies occurs primarily in areas**
641 **with pronounced heterogeneity, and this energy distribution is uneven across the region**
642 **(Aubinet et al., 2012). Once large-scale eddies acquire energy, their cascading of energy**
643 **to smaller-scale eddies is influenced by topographic features, leading to variations in**
644 **these smaller-scale eddies along different flow streams (Chen et al., 2023).** In complex
645 terrains, the bidirectional airflow within forests along slopes can cause the decoupling
646 of soil CO_2 fluxes from EC measurements above the forest canopy (Feigenwinter et al.,
647 2008; Aubinet et al., 2003), leading to significant errors in CO_2 flux measurements.
648 Forest soil serves as the primary source of CO_2 gas and regions of high flux over
649 complex terrains act like chimneys, transporting air parcels from the soil surface within
650 forests (Chen et al., 2019). **By increasing the number of gas concentration sampling**
651 **points near the ground, the horizontal representativeness can be enhanced, thereby**
652 **reducing the bias in the estimation of F_s (Nicolini et al., 2018).** In situations where
653 turbulence is not well-developed, and CO_2 mixing is inadequate, the trend of F_s with
654 turbulence intensity aligns with that of advective fluxes, which is opposite to that of
655 turbulent fluxes (Mchugh et al., 2017). The temporal dynamics and amplitudes of F_s

656 changes are influenced by topography complexity and wind conditions above the forest
657 canopy (Fig. 10). Locations with more complex and sloping topography at the flux
658 tower are more likely to generate advective fluxes that may not be easily observed at a
659 single point.

660 Estimating landscape CO₂ fluxes in complex terrains solely based on
661 measurements from a single flux tower can introduce significant errors and biases that
662 are not acceptable. The magnitude of these errors in F_s estimates is dependent on the
663 height of the forest canopy and the endogenous source/sink (Chen et al., 2020). To
664 mitigate errors and biases associated with estimating F_s in complex terrains, we
665 employed a regression modeling approach using the decision-level fusion model. This
666 method involves computing a weighted average of F_s based on different [CO₂]
667 averaging time windows, effectively reducing errors and biases in the estimation of F_s
668 (see Table 5). In fact, from the definition of storage flux, it can be seen that weighting
669 the storage flux is essentially weighting the [CO₂] in the average time window, which
670 means replacing spatial sequences with temporal sequences for weighting. The
671 weighting coefficients used to construct the model were based on the relative errors and
672 biases of F_s estimation, with the weighting coefficient decreasing as the represented
673 moment's length increased. To obtain more accurate estimates of forest ecosystem F_s in
674 complex terrains, further research should focus on understanding the spatiotemporal
675 patterns and dynamics of [CO₂].

676 **5 Conclusions**

677 This study investigated the impact of short-term [CO₂] fluctuations on the
678 estimation of F_s in temperate forest ecosystems within complex terrains. Additionally,
679 it examined the F_s uncertainty and the contribution of the F_s to NEE using data from
680 three flux towers. To enhance F_s uncertainty estimation, statistical sampling techniques
681 were applied based on the individual tower approach.

682 The results highlighted the significance of considering multiple time windows for
683 averaging [CO₂] when estimating F_s, as [CO₂] above the forest canopies exhibited
684 fluctuations with periods ranging from 1 to 10 minutes. Diurnal, seasonal, and spatial
685 variations were observed in the amplitude and periodicity of [CO₂] fluctuations,
686 highlighting the need for thoughtful sampling strategies. The use of individual gas
687 analyzers to sample the CO₂ in the control volume was inadequate, leading to
688 systematic biases and random errors in the F_s estimates. Increasing [CO₂] averaging
689 time windows mitigated the effect of [CO₂] fluctuations on F_s estimates, reducing both
690 their magnitude and uncertainty.

691 The study also revealed that the uncertainty of F_s followed a non-normal
692 distribution, with its standard deviation positively correlated with F_s magnitude, which
693 has important implications for quality control. To improve F_s estimation, a decision-
694 level fusion model was introduced, integrating F_s estimates from multiple [CO₂]
695 averaging time windows, effectively reducing the impact of short-term [CO₂]
696 fluctuations while considering underestimation bias and random errors. The
697 contribution of F_s to NEE exhibited diurnal, seasonal, and spatial variations associated

698 with u^* , contributing to the NEE observations at rates ranging from 17.2% to 82.0%
699 depending on the turbulent mixing and terrain complexity. The influence of terrain
700 complexity on the relationship between $[\text{CO}_2]$ fluctuations, turbulent mixing, and the
701 contribution of F_s to NEE was also evident. The findings from the three flux towers
702 allowed for the generalization of these results beyond the study site. These insights
703 provide crucial scientific support for the practical application of the eddy covariance
704 technique and advance our understanding of accurately estimating NEE in forest
705 ecosystems in complex terrains.

706 **Appendix A**

707 *A.1 the weight parameters of the decision-level fusion model*

708 For each 30-min CO_2 storage flux (F_s) estimate based on the CO_2 concentration
709 ($[\text{CO}_2]$) averaging time window (τ), the weight in the decision-level fusion model can
710 be obtained by weighting the random uncertainty and bias of F_{s_τ} .

711 The weight of the random uncertainty for the F_{s_τ} is expressed as follows:

$$w_\tau = \frac{1/\sigma(\varepsilon_\tau)}{\sum_j 1/\sigma(\varepsilon_j)}, \quad (\text{A.1})$$

712 where $\sigma(\varepsilon_\tau)$ is the random uncertainty of the F_{s_τ} , qualified as the standard deviation.

713 The weight of the bias for the F_{s_τ} is expressed as follows:

$$W_\tau = \frac{K_\tau}{\sum_j K_j}, \quad (\text{A.2})$$

714 where K_τ is the slope between the F_{s_τ} and $F_{s_{28}}$.

715 Ultimately, the weight of the F_{s_τ} in the decision-level fusion model can be
716 calculated using the following equation:

$$w_{\tau}^* = rw_{\tau} + (1 - r)W_{\tau}, \quad (\text{A.3})$$

717 where r represents the proportion of the weight of random uncertainty.

718 A.2 Complex terrain index

719 This study employed a novel descriptor called the terrain complexity index (*TCI*)
 720 to quantify the complexity of the three-dimensional terrain. For a given unit area, the
 721 *TCI* equation can be expressed as follows:

$$TCI = (1 - P_d \cos \alpha_d)(1 - Z_d^{-1})(D_f - 2)^{-H/\ln(12)}, \quad (\text{A.4})$$

722 where, P_d represents the volume of terrain above the lowest elevation of an area
 723 unit (V_u) divided by the product of its largest vertically projected area (S_v) and the
 724 edge length of the side of the area unit (d), expressed as $P_d = V_u/(S_v d)$; P_d was
 725 defined to be one when the S_v is zero. **Given V_u , an increase in S_v correlates with a**
 726 **higher degree of terrain complexity. Notably, the P_d is defined as 1 when the terrain**
 727 **volume is 0 or when the terrain surface of the area unit was parallel to the horizontal**
 728 **plane and was smooth and homogeneous.** α_d indicates the slope of the area unit. Z_d
 729 denoted the terrain roughness, which defined as the ratio of the terrain surface area to
 730 the projected horizontal plane (Loke and Chisholm, 2022). **The value of Z_d is in the**
 731 **range of $[1, +\infty)$. The larger Z_d , the more complex the terrain.** D_f is the fractal
 732 dimension of terrain surface area, which ranged from 2 to 3 and described the
 733 complexity in spatially self-similar structure of the local surface within the area unit
 734 and the area unit surface (B. B. Mandelbrot, 1967; Taud and Parrot, 2005). Employing
 735 terrain surface area, the box-counting method is used to estimate fractal dimension of
 736 unit area. H represented the Shannon-Wiener index and expressed as $H =$

737 $-\sum_{i=1}^n P_i \ln(P_i)$, capturing the uniformity of the spatial distribution of the pixel
738 aspects within the area unit (Brown, 1997). When the aspect of each pixel is divided
739 into 30° segments, P_i denotes the proportion of the i^{th} type of pixel aspects within the
740 area unit and n was the total number of pixel aspect types within the area unit. A
741 larger H indicates a more complex terrain. When the number of pixel aspect types in
742 the area unit is kept constant, it's essential to recognize that greater uniformity in the
743 distribution of all pixel aspect in the area unit results in a larger H . Similarly, when the
744 uniformity of the distribution of pixel aspects in the area unit is kept constant, a larger
745 H is achieved with an increase in the observation of the number of pixel aspect types.

746 To quantify the terrain complexity of the underlying surface around the flux towers,
747 we computed the quartiles of TCI for all area units within a sector (divided by 30°) with
748 a radius of 380 m. A weighted geometric mean was employed to construct $TCIs$, which
749 describe the statistical distribution of TCI of the sector. The $TCIs$ represents the
750 topographic complexity of the sector and are calculated using the following equation:

$$751 \quad TCI_s = (TCI_5 TCI_{25} TCI_{50} TCI_{75} TCI_{95})^{1/5} \quad (\text{A.5})$$

752 where TCI_5 , TCI_{25} , TCI_{50} , TCI_{75} , and TCI_{95} are the quartiles of 5%, 25%, 50%, 75%,
753 and 95%, respectively. The $TCIs$ values range from 0 to 1, with higher values indicating
754 greater terrain complexity.

755 *Data availability.* Data used in this paper are available at the Science Data Bank
756 (<https://www.scidb.cn/en/s/7ZfQZv>) or upon request to the corresponding author.

757 *Author contributions.* DT developed the manuscript; JZ was responsible for
758 conceptualizing the idea and designing the research study; TG substantially structured

759 the manuscript; FY contributed to the data collection process; YZ helped in the design
760 and preparation of the figures and tables; XZ and BY revised the manuscript.

761 *Competing interests.* The authors declare that they have no known competing
762 financial interests or personal relationships that could have appeared to influence the
763 work reported in this paper.

764 *Acknowledgments.* We are grateful to Qingyuan Forest CERN, Chinese Academy of
765 Sciences/Qingyuan Forest, National Observation and Research Station, Liaoning
766 Province, China for providing forest sites, instrument systems, and logistic supports.

767 *Financial support.* This research was financially supported by the National Natural
768 Science Foundation of China (No. 32192435), the China Postdoctoral Science
769 Foundation (No. 2023M733672), **Key R&D Program of Liaoning Province**
770 **(2023JH2/101800043)**, and the Postdoctoral Research Startup Foundation of Liaoning
771 Province of China (No. 2022-BS-022).

772 **Reference**

773 Aubinet, M., Heinesch, B., and Yernaux, M.: Horizontal and Vertical CO₂ Advection In A Sloping Forest,
774 Boundary-Layer Meteorology, 108, 397-417, 10.1023/a:1024168428135, 2003.

775 Aubinet, M., Vesala, T., and Papale, D.: Eddy Covariance: A Practical Guide to Measurement and Data
776 Analysis, Springer Atmospheric Sciences, Springer, Dordrecht, XXII, 438 pp., 10.1007/978-94-007-
777 2351-1, 2012.

778 Aubinet, M., Grelle, A., Ibrom, A., Rannik, Ü., Moncrieff, J., Foken, T., Kowalski, A. S., Martin, P. H.,
779 Berbigier, P., Bernhofer, C., Clement, R., Elbers, J., Granier, A., Grünwald, T., Morgenstern, K.,
780 Pilegaard, K., Rebmann, C., Snijders, W., Valentini, R., and Vesala, T.: Estimates of the Annual Net
781 Carbon and Water Exchange of Forests: The EUROFLUX Methodology, in: Advances in Ecological
782 Research Volume 30, Advances in Ecological Research, 113-175, 10.1016/s0065-2504(08)60018-5,
783 2000.

784 B. B. Mandelbrot: How Long Is the Coast of Britain? Statistical Self-Similarity and Fractional Dimension,
785 Science, 156, 636-638, 1967.

786 Belušić, D. and Mahrt, L.: Is geometry more universal than physics in atmospheric boundary layer flow?,
787 Journal of Geophysical Research: Atmospheres, 117, n/a-n/a, 10.1029/2011jd016987, 2012.

788 Bjorkegren, A. B., Grimmond, C. S. B., Kotthaus, S., and Malamud, B. D.: CO₂ emission estimation in

789 the urban environment: Measurement of the CO₂ storage term, *Atmospheric Environment*, 122, 775-790,
790 10.1016/j.atmosenv.2015.10.012, 2015.

791 Brown, S.: Estimating Biomass and Biomass Change of Tropical Forests: A Primer, *FAO Forestry Paper*,
792 134, 1997.

793 Cava, D., Giostra, U., Siqueira, M., and Katul, G.: Organised motion and radiative perturbations in the
794 nocturnal canopy sublayer above an even-aged pine forest, *Boundary-Layer Meteorology*, 112, 129-157,
795 DOI 10.1023/B:BOUN.0000020160.28184.a0, 2004.

796 Cescatti, A., Marcolla, B., Goded, I., and Gruening, C.: Optimal use of buffer volumes for the
797 measurement of atmospheric gas concentration in multi-point systems, *Atmospheric Measurement*
798 *Techniques*, 9, 4665-4672, 10.5194/amt-9-4665-2016, 2016.

799 Chen, B., Chamecki, M., and Katul, G. G.: Effects of topography on in-canopy transport of gases emitted
800 within dense forests, *Quarterly Journal of the Royal Meteorological Society*, 145, 2101-2114,
801 10.1002/qj.3546, 2019.

802 Chen, B. C., Chamecki, M., and Katul, G. G.: Effects of Gentle Topography on Forest-Atmosphere Gas
803 Exchanges and Implications for Eddy-Covariance Measurements, *J Geophys Res-Atmos*, 125, ARTN
804 e2020JD032581
805 10.1029/2020JD032581, 2020.

806 Chen, J., Chen, X., Jia, W., Yu, Y., and Zhao, S.: Multi-sites observation of large-scale eddy in surface
807 layer of Loess Plateau, *Science China Earth Sciences*, 66, 871–881, [https://doi.org/10.1007/s11430-022-](https://doi.org/10.1007/s11430-022-1035-4)
808 [1035-4](https://doi.org/10.1007/s11430-022-1035-4), 2023.

809 de Araújo, A. C., J.P.H.B., O., Dolman, A. J., B., K., M.J., W., and J.R., E.: Implications of CO₂ pooling
810 on delta C13 of ecosystem respiration and leaves in Amazonian forest, *Biogeosciences*, 5, 779-795,
811 10.5194/bg-5-779-2008, 2008.

812 de Araújo, A. C., Dolman, A. J., Waterloo, M. J., Gash, J. H. C., Kruijt, B., Zanchi, F. B., de Lange, J. M.
813 E., Stoevelaar, R., Manzi, A. O., Nobre, A. D., Lootens, R. N., and Backer, J.: The spatial variability of
814 CO₂ storage and the interpretation of eddy covariance fluxes in central Amazonia, *Agricultural and Forest*
815 *Meteorology*, 150, 226-237, 10.1016/j.agrformet.2009.11.005, 2010.

816 Edburg, S. L., Stock, D., Lamb, B. K., and Patton, E. G.: The Effect of the Vertical Source Distribution
817 on Scalar Statistics within and above a Forest Canopy, *Boundary-Layer Meteorology*, 142, 365-382,
818 10.1007/s10546-011-9686-1, 2011.

819 Feigenwinter, C., Bernhofer, C., and Vogt, R.: The Influence of Advection on the Short Term CO₂-Budget
820 in and Above a Forest Canopy, *Boundary-Layer Meteorology*, 113, 201-224,
821 10.1023/B:BOUN.0000039372.86053.ff, 2004.

822 Feigenwinter, C., Bernhofer, C., Eichelmann, U., Heinesch, B., Hertel, M., Janous, D., Kolle, O.,
823 Lagergren, F., Lindroth, A., Minerbi, S., Moderow, U., Mölder, M., Montagnani, L., Queck, R., Rebmann,
824 C., Vestin, P., Yernaux, M., Zeri, M., Ziegler, W., and Aubinet, M.: Comparison of horizontal and vertical
825 advective CO₂ fluxes at three forest sites, *Agricultural and Forest Meteorology*, 148, 12-24,
826 10.1016/j.agrformet.2007.08.013, 2008.

827 Finnigan, J.: The storage term in eddy flux calculations, *Agricultural and Forest Meteorology*, 136, 108-
828 113, 10.1016/j.agrformet.2004.12.010, 2006.

829 Finnigan, J., Ayotte, K., Harman, I., Katul, G., Oldroyd, H., Patton, E., Poggi, D., Ross, A., and Taylor,
830 P.: Boundary-Layer Flow Over Complex Topography, *Boundary-Layer Meteorology*, 177, 247-313,
831 10.1007/s10546-020-00564-3, 2020.

832 Fuentes, J. D., Wang, D., Bowling, D. R., Potosnak, M., Monson, R. K., Goliff, W. S., and Stockwell, W.

833 R.: Biogenic Hydrocarbon Chemistry within and Above a Mixed Deciduous Forest, *Journal of*
834 *Atmospheric Chemistry*, 56, 165-185, 10.1007/s10874-006-9048-4, 2006.

835 Gao, T., Yu, L.-Z., Yu, F.-Y., Wang, X.-C., Yang, K., Lu, D.-L., Li, X.-F., Yan, Q.-L., Sun, Y.-R., Liu, L.-
836 F., Xu, S., Zhen, X.-J., Ni, Z.-D., Zhang, J.-X., Wang, G.-F., Wei, X.-H., Zhou, X.-H., and Zhu, J.-J.:
837 Functions and applications of Multi-Tower Platform of Qingyuan Forest Ecosystem Research Station of
838 Chinese Academy of Sciences, *Chinese journal of applied ecology*, 31, 695-705, 10.13287/j.1001-
839 9332.202003.040, 2020.

840 Gerken, T., Chamecki, M., and Fuentes, J. D.: Air-Parcel Residence Times Within Forest Canopies,
841 *Boundary-Layer Meteorology*, 165, 29-54, 10.1007/s10546-017-0269-7, 2017.

842 Grant, E. R., Ross, A. N., Gardiner, B. A., and Mobbs, S. D.: Field Observations of Canopy Flows over
843 Complex Terrain, *Boundary-Layer Meteorology*, 156, 231-251, 10.1007/s10546-015-0015-y, 2015.

844 Gu, L., Massman, W. J., Leuning, R., Pallardy, S. G., Meyers, T., Hanson, P. J., Riggs, J. S., Hosman, K.
845 P., and Yang, B.: The fundamental equation of eddy covariance and its application in flux measurements,
846 *Agricultural and Forest Meteorology*, 152, 135-148, 10.1016/j.agrformet.2011.09.014, 2012.

847 Heinesch, B., Yernaux, M., and Aubinet, M.: Some methodological questions concerning advection
848 measurements: a case study, *Boundary-Layer Meteorology*, 122, 457-478, 10.1007/s10546-006-9102-4,
849 2007.

850 Hollinger, D. Y. and Richardson, A. D.: Uncertainty in eddy covariance measurements and its application
851 to physiological models, *Tree Physiol*, 25, 873-885, DOI 10.1093/treephys/25.7.873, 2005.

852 Huang, N. E., Shen, Z., Long, S. R., Wu, M. C., Shih, H. H., Zheng, Q., Yen, N.-C., Tung, C. C., and Liu,
853 H. H.: The empirical mode decomposition and the Hilbert spectrum for nonlinear and non-stationary
854 time series analysis, *Proceedings of the Royal Society of London. Series A: Mathematical, Physical and*
855 *Engineering Sciences*, 454, 903-995, 10.1098/rspa.1998.0193, 1998.

856 Khélifa, N., Lecollinet, M., and Himbert, M.: Molar mass of dry air in mass metrology, *Measurement*,
857 40, 779-784, 10.1016/j.measurement.2006.05.009, 2007.

858 Leuning, R., Zegelin, S. J., Jones, K., Keith, H., and Hughes, D.: Measurement of horizontal and vertical
859 advection of CO₂ within a forest canopy, *Agricultural and Forest Meteorology*, 148, 1777-1797,
860 10.1016/j.agrformet.2008.06.006, 2008.

861 Li, S., Yan, Q., Liu, Z., Wang, X., Yu, F., Teng, D., Sun, Y., Lu, D., Zhang, J., Gao, T., and Zhu, J.:
862 Seasonality of albedo and fraction of absorbed photosynthetically active radiation in the temperate
863 secondary forest ecosystem: A comprehensive observation using Qingyuan Ker towers, *Agricultural and*
864 *Forest Meteorology*, 333, 10.1016/j.agrformet.2023.109418, 2023.

865 Li, Y.-C., Liu, F., Wang, C.-K., Gao, T., and Wang, X.-C.: Carbon budget estimation based on different
866 methods of CO₂ storage flux in forest ecosystems, *Chinese journal of applied ecology*, 31, 3665-3673,
867 10.13287/j.1001-9332.202011.004, 2020.

868 Loke, L. H. L. and Chisholm, R. A.: Measuring habitat complexity and spatial heterogeneity in ecology,
869 *Ecology Letters*, 25, 2269-2288, 10.1111/ele.14084, 2022.

870 Marcolla, B., Cobbe, I., Minerbi, S., Montagnani, L., and Cescatti, A.: Methods and uncertainties in the
871 experimental assessment of horizontal advection, *Agricultural and Forest Meteorology*, 198-199, 62-71,
872 10.1016/j.agrformet.2014.08.002, 2014.

873 McHugh, I. D., Beringer, J., Cunningham, S. C., Baker, P. J., Cavagnaro, T. R., Mac Nally, R., and
874 Thompson, R. M.: Interactions between nocturnal turbulent flux, storage and advection at an "ideal"
875 eucalypt woodland site, *Biogeosciences*, 14, 3027-3050, 10.5194/bg-14-3027-2017, 2017.

876 McMaster, G. S. and Wilhelm, W. W.: Growing degree-days: one equation, two interpretations,

877 Agricultural and Forest Meteorology, 87, 291-300, Doi 10.1016/S0168-1923(97)00027-0, 1997.

878 Metzger, S.: Surface-atmosphere exchange in a box: Making the control volume a suitable representation
879 for in-situ observations, Agricultural and Forest Meteorology, 255, 68-80,
880 10.1016/j.agrformet.2017.08.037, 2018.

881 Montagnani, L., Grunwald, T., Kowalski, A., Mammarella, I., Merbold, L., Metzger, S., Sedlak, P., and
882 Siebicke, L.: Estimating the storage term in eddy covariance measurements: the ICOS methodology, Int
883 Agrophys, 32, 551-567, 10.1515/intag-2017-0037, 2018.

884 Montagnani, L., Manca, G., Canepa, E., Georgieva, E., Acosta, M., Feigenwinter, C., Janous, D.,
885 Kerschbaumer, G., Lindroth, A., Minach, L., Minerbi, S., Mölder, M., Pavelka, M., Seufert, G., Zeri, M.,
886 and Ziegler, W.: A new mass conservation approach to the study of CO₂ advection in an alpine forest,
887 Journal of Geophysical Research, 114, 10.1029/2008jd010650, 2009.

888 Nadeau, D. F., Parodyjak, E. R., Higgins, C. W., Huwald, H., and Parlange, M. B.: Flow during the evening
889 transition over steep Alpine slopes, Quarterly Journal of the Royal Meteorological Society, 139, 607-624,
890 10.1002/qj.1985, 2013.

891 Nicolini, G., Aubinet, M., Feigenwinter, C., Heinesch, B., Lindroth, A., Mamadou, O., Moderow, U.,
892 Mölder, M., Montagnani, L., Rebmann, C., and Papale, D.: Impact of CO₂ storage flux sampling
893 uncertainty on net ecosystem exchange measured by eddy covariance, Agricultural and Forest
894 Meteorology, 248, 228-239, 10.1016/j.agrformet.2017.09.025, 2018.

895 Richardson, A. D., Hollinger, D. Y., Burba, G. G., Davis, K. J., Flanagan, L. B., Katul, G. G., William
896 Munger, J., Ricciuto, D. M., Stoy, P. C., Suyker, A. E., Verma, S. B., and Wofsy, S. C.: A multi-site
897 analysis of random error in tower-based measurements of carbon and energy fluxes, Agricultural and
898 Forest Meteorology, 136, 1-18, 10.1016/j.agrformet.2006.01.007, 2006.

899 Richardson, A. D., Mahecha, M. D., Falge, E., Kattge, J., Moffat, A. M., Papale, D., Reichstein, M.,
900 Stauch, V. J., Braswell, B. H., Churkina, G., Kruijt, B., and Hollinger, D. Y.: Statistical properties of
901 random CO₂ flux measurement uncertainty inferred from model residuals, Agricultural and Forest
902 Meteorology, 148, 38-50, 10.1016/j.agrformet.2007.09.001, 2008.

903 Sha, J., Zou, J., and Sun, J.: Observational study of land-atmosphere turbulent flux exchange over
904 complex underlying surfaces in urban and suburban areas, SCIENCE CHINA-EARTH SCIENCES, 64,
905 1050-1064, 10.1007/s11430-020-9783-2, 2021.

906 Siebicke, L., Steinfeld, G., and Foken, T.: CO₂-gradient measurements using a parallel multi-analyzer
907 setup, Atmospheric Measurement Techniques, 4, 409-423, 10.5194/amt-4-409-2011, 2011.

908 Taud, H. and Parrot, J.-F.: Measurement of DEM roughness using the local fractal dimension,
909 Géomorphologie : relief, processus, environnement, 11, 327-338, 10.4000/geomorphologie.622, 2005.

910 van Gorsel, E., Harman, I. N., Finnigan, J. J., and Leuning, R.: Decoupling of air flow above and in plant
911 canopies and gravity waves affect micrometeorological estimates of net scalar exchange, Agricultural
912 and Forest Meteorology, 151, 927-933, 10.1016/j.agrformet.2011.02.012, 2011.

913 Wang, J., Shi, T., Yu, D., Teng, D., Ge, X., Zhang, Z., Yang, X., Wang, H., and Wu, G.: Ensemble
914 machine-learning-based framework for estimating total nitrogen concentration in water using drone-
915 borne hyperspectral imagery of emergent plants: A case study in an arid oasis, NW China, Environmental
916 Pollution, 266, 10.1016/j.envpol.2020.115412, 2020.

917 Wang, X., Wang, C., Guo, Q., and Wang, J.: Improving the CO₂ storage measurements with a single
918 profile system in a tall-dense-canopy temperate forest, Agricultural and Forest Meteorology, 228-229,
919 327-338, 10.1016/j.agrformet.2016.07.020, 2016.

920 Warton, D. I., Duursma, R. A., Falster, D. S., and Taskinen, S.: smatr 3- an R package for estimation and

921 inference about allometric lines, *Methods in Ecology and Evolution*, 3, 257-259, 10.1111/j.2041-
922 210X.2011.00153.x, 2012.

923 Webb, E. K., Pearman, G. I., and Leuning, R.: Correction of flux measurements for density effects due
924 to heat and water vapour transfer, *Quarterly Journal of the Royal Meteorological Society*, 106, 85-100,
925 10.1002/qj.49710644707, 1980.

926 Xu, K., Pingingtha-Durden, N., Luo, H., Durden, D., Sturtevant, C., Desai, A. R., Florian, C., and Metzger,
927 S.: The eddy-covariance storage term in air: Consistent community resources improve flux measurement
928 reliability, *Agricultural and Forest Meteorology*, 279, 10.1016/j.agrformet.2019.107734, 2019.

929 Yang, B., Hanson, P. J., Riggs, J. S., Pallardy, S. G., Heuer, M., Hosman, K. P., Meyers, T. P., Wullschleger,
930 S. D., and Gu, L.-H.: Biases of CO₂ storage in eddy flux measurements in a forest pertinent to vertical
931 configurations of a profile system and CO₂ density averaging, *Journal of Geophysical Research*, 112,
932 10.1029/2006jd008243, 2007.

933 Yang, P. C., Black, T. A., Neumann, H. H., Novak, M. D., and Blanken, P. D.: Spatial and temporal
934 variability of CO₂ concentration and flux in a boreal aspen forest, *J Geophys Res-Atmos*, 104, 27653-
935 27661, Doi 10.1029/1999jd900295, 1999.

936 Yao, Y., Zhang, Y., Yu, G., Song, Q., Tan, Z., and Zhao, J.: Estimation of CO₂ storage flux between forest
937 and atmosphere in a tropical forest, *Journal of Beijing Forestry University*, 33, 23-29, 2011.

938 Zhang, M., Wen, X., Yu, G.-r., Zhang, L.-m., Fu, Y., Sun, X., and Han, S.-j.: Effects of CO₂ storage flux
939 on carbon budget of forest ecosystem, *Chinese journal of applied ecology*, 21, 1201-1209, 2010.

940 Zhu, J., Gao, T., Yu, L., Yu, F., Yang, K., Lu, D., Yan, Q., Sun, Y., Liu, L., Xu, S., Zhang, J., Zheng, X.,
941 Song, L., and Zhou, X.: Functions and Applications of Multi-tower Platform of Qingyuan Forest
942 Ecosystem Research Station of Chinese Academy of Sciences (Qingyuan Ker Towers), *Bulletin of the*
943 *Chinese Academy of Sciences*, 36, 351-361, 10.16418/j.issn.1000-3045.20210304002, 2021.